INSTABILITY OF PREMIXED LEAN HYDROGEN LAMINAR TUBULAR FLAMES

By

Carl Alan Hall

Dissertation

Submitted to the Faculty of the

Graduate School of Vanderbilt University

in partial fulfillment of the requirements

for the degree of

DOCTOR OF PHILOSOPHY

in

Mechanical Engineering

May, 2016

Nashville, Tennessee

Approved:

Professor Robert W. Pitz, Chair

Professor M. Douglas LeVan

Professor Haoxiang Luo

Professor A. V. Anilkumar

Professor Deyu Li

ACKNOWLEDGMENTS

I would like to thank my adviser, Dr. Robert Pitz, for his support and advice, particularly during the high-risk and time-intensive development phase of the numerical simulation code. Without his patience and guidance, this investigation could not have told the complete story of premixed tubular cellular phenomena.

I would also like to thank the patience and expertise of Spectral Energies research scientists Dr.'s Waruna Kulatilaka and Naibo Jiang, as well as Dr.'s Jim Gord and Sukesh Roy. Without their help, the measurements of minor species would not have been possible at such speed and high quality.

Finally, I would like to thank fellow graduate students Marc Ramsey and Nathan Grady for their helpful critiques of my work, as well as Darren Tinker for his suggestions for modifications to the numerical simulation code. It goes without saying that the numerical portion of this work would not be possible without the time and commitment of numerous other students and research staff world wide actively contributing to public domain scientific computing software.

This work was primarily supported by the National Science Foundation under Grant CBET-1134268. Collaboration with the Spectral Energies research staff was supported by Air Force Office of Scientific Research (Dr. Chiping Li, Program Manager) and the Air Force Research Laboratory under Contract No. FA8650-12-C-2200.

TABLE OF CONTENTS

LIST OF FIGURES

LIST OF TABLES

NOMENCLATURE

A	spontaneous transition rate (s^{-1})
c_p	specific heat of mixture (erg/g-K)
C	experimental calibration factor
$\mathcal{D}$	diffusion coefficient matrix (g/cm-s)
E	average laser pulse energy (mJ)
f_b	Boltzmann factor
h	specific enthalpy (erg/g)
H	pressure eigenvalue (Ba/cm^2)
I	radial and azimuthal pressure (Ba)
$\mathbf{j}$	species mass flux (g/cm^2-s)
J	rotational level
k	stretch rate (s^{-1})
k_b	Boltzmann constant (erg/K)
K	Raman calibration matrix (cm^3/mJ)
m	mean molar mass (g/mole)
N	number density (cm^{-3})

	Greek Letters
$\boldsymbol{\delta}$	identity matrix
θ	azimuthal coordinate (rad)
κ	dilational viscosity (g/cm-s)
λ	heat conductivity (erg/cm-K-s)
μ	viscosity of mixture (g/cm-s)
ν	vibrational level
p_0	thermodynamic pressure (Ba)
$\widetilde{p}_1$	lumped perturbed pressure (Ba)
q	heat flux (erg/cm^2-s)
Q	radiation heat loss (erg/cm^3-s)
	collisional quenching rate (s^{-1})
r	radial coordinate (cm)
R	outer nozzle diameter (cm)
S	experimentally collected signal
$\mathcal{S}$	Set of chemical species
T	temperature (K)
u	radial velocity component (cm/s)
v	azimuthal velocity component (cm/s)
W	axial velocity gradient (s^{-1})
x	mole fraction
Y	mass fraction
z	axial coordinate (cm)
ρ	density (g/cm^3)
$\boldsymbol{\sigma}$	momentum flux (g/cm-s^2)
Φ	equivalence ratio
χ	thermal diffusion ratio
ω	species production rate (mole/cm^3-s)

	Superscripts
d	diffusion velocity
D	Dufour effect
T	Soret effect

	Subscripts
BC	Boundary condition value

CHAPTER I

INTRODUCTION

The complete understanding of combustion remains intractable due to the conditions found in practical applications (e.g. high pressure, high intensity turbulence, high molecular weight fuel mixtures). This complexity is successfully mitigated for numerical simulation approaches through the use of computationally efficient models that approximate the problem physics: e.g. using large-eddy simulation for the velocity field [1], flamelet manifolds for the chemical kinetics [2], or a mixture-averaged form for diffusive transport [3]. Limitations arise in the methodology for validating these modeling approximations, due to the inability to experimentally measure the required quantities combined with the excessive numerical cost of performing detailed simulations.

Laminar flames offer a compromise to this problem by being less realistic at the gain of better accessibility through detailed numerical and quantitative experimental characterization. These data sets can be used to support chemistry and transport model validation [4]. Laminar flames sustained in carefully designed burners provide structure with reduced spatial dimensionality (e.g. 1D or 2D) and may be held time-steady. These aspects greatly reduce the computational requirements, permitting full detailed numerical experiments to directly validate modeling approximations. The intent of this work is to investigate a laminar flame geometry that has good experimental and numerical access that exhibits structure similar to practical turbulent flames.

Cellular flames offer this capability by creating a flame surface with varying curvature, localized extinction zones, and enhanced reaction cells. The common cause for this structure is an imbalance between the diffusive heat and mass fluxes [5], suggesting that simulations of cellular flame structures will be highly sensitive to the accuracy of diffusive

transport modeling approximations. And by investigating this flame type in a tubular flowfield [6], the cells exhibit 2D time independent planar structure with good spatial symmetry [7]. This significantly reduces the experimental and numerical cost of characterization, and yet the relative complexity of the flame surface allows for a strong test of modeling assumptions.

This investigation will focus on the dual experimental and numerical characterization of time steady premixed cellular tubular flames in dilute, lean hydrogen mixtures. The experimental approach will provide spatially resolved and quantitative measurements of temperature, major species, and two minor species (H and OH) through flame cross-sections. The numerical approach will provide predicted flame structure including full detailed chemical kinetics and multicomponent transport. With these results, (1) the structure of cellular tubular flames will be characterized and discussed, and (2) the ability for cellular flame studies to impact investigations of practical flames is examined.

1.1 Background

Premixed flames are reaction waves that propagate through a mixture of fuel and oxidizer. The chemical structure of these flames is usually discussed in terms of the normalized fuel-oxidizer ratio, *equivalence ratio*,

$$\Phi = \left(\frac{x_f}{x_o}\right) \Big/ \left(\frac{x_f}{x_o}\right)_{st} \tag{1.1}$$

where x_f is the fuel mole fraction, x_o is the oxidizer mole fraction, and the denominator is the stoichiometric fuel-oxidizer ratio. The equivalence ratio is unity for stiochiometric flames, sub-unity for lean flames, and greater than unity for rich flames.

Flames are characterized chemically by a chain reaction mechanism composed of two types of species: intermediate radicals that characterize the flame in the reaction zone (e.g. H, O, OH, HO_2, H_2O_2), and major species that define the overall structure flame and

flow field (e.g. H_2, O_2, H_2O). The rate of reaction is large, and the formation of some intermediate species is higher than predicted by thermodynamic theory—compounds are created in excited electronic states that relax back into thermal-equilibrium levels with the emission of photons (chemiluminescence). Imaging of this emission is valuable to qualitatively understand the structure of reaction zones, and distinguishes the reaction zones from cold gas and hot products.

1.1.1 Flame Stretch

The effect of the flow field on flame structure is discussed in terms of the local strain rate at the flame surface. This *stretch rate* is the extension or compression of the flame sheet and is important for flame extinction, which occurs in practical combustors for large positive stretch [8]. In the simplest description of a flame, the thickness of the reaction layer is thin compared to the characteristic dimension of the flow field. This assumption allows the flame to be treated as an infinitely thin sheet, and the stretch rate is simply defined as,

$$k = \frac{1}{A}\frac{dA}{dt} \tag{1.2}$$

where A is the unit area of the flame. To calculate stretch for realistic flames with finite thickness, stretch is more conveniently expressed in terms of primitive variables [9],

$$k = \frac{1}{\rho}\nabla \cdot \left(\rho \boldsymbol{u}_{\parallel}\right) \tag{1.3}$$

where $\boldsymbol{u}_{\parallel}$ is the velocity field parallel to the flame orientation (e.g. defined in reference [10]).

1.1.2 Stagnation-Point Flow Fields

The tubular flow field is a type of stagnation-point flow field. This class of flow fields has been utilized for decades due to presence of a similarity-type solution (also referred to

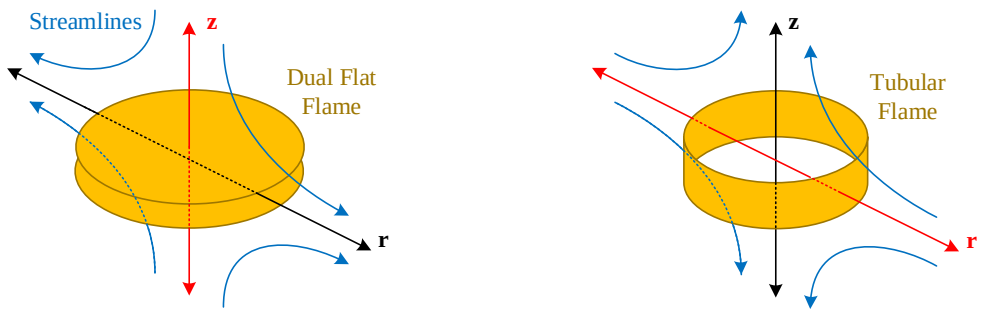

Figure 1.1 Schematic of non-cellular flame geometry in an axially opposed (left) and radially opposed "tubular" (right) jet burner.

as a boundary layer assumption [11]) to express scalar fields (i.e. flames) as 1D within the 2D axisymmetric velocity field. Experimentally, the flow field is created by opposed inlet nozzles, spaced equidistantly from the coordinate origin. The configuration of the jets defines the flame geometry: radially opposed jets create a tubular curved flame, and axially opposed jets create twin flat flames. Simplified schematics of the flow fields created by these two burners is shown in Figure 1.1.

An inviscid constant density solution to the governing equations provides valuable insight to the physical problem. With the assumptions of axisymmetry, nozzles placed at a finite distance, and a known flame orientation, the flame stretch rate may be expressed in analytical form [12]. For the tubular flame, the flow field is defined over $r \in [0, R]$ and the stretch rate is expressed as,

$$k = |u_{BC}| \frac{\pi}{R} \cos\left(\frac{\pi}{2}\frac{r^2}{R^2}\right) \tag{1.4}$$

where u_{BC} is the radial velocity at the nozzle boundary radius R, and the absolute value operator is used to emphasize the experimental operating conditions (negative radial velocities and positive stretch rates). The resulting form of the stretch rate is advantageous experimentally: at short radii the stretch rate is nearly independent of the radial coordinate

and can be approximated as a function of only the boundary conditions:

$$k \approx |u_{BC}| \frac{\pi}{R} \tag{1.5}$$

1.2 Tubular Flames

Investigations of tubular flames are commonly performed to examine the combined effects of curvature and stretch on flame structure [6, 13]. The curvature of the flow field causes H_2-air non-cellular tubular flames to have higher peak temperatures and to extinguish at much higher stretch rates as compared to flat opposed jet flames with the same inlet mixture. Good agreement is found between experimental measurements and simulations performed using the stagnation-point similarity solution for non-cellular tubular flames [14].

1.2.1 Cellular Flame Structure

The tubular geometry is ideal for investigations of cellular flames. Observations of chemiluminescence show that the cellular structure is strongly azimuthally symmetric and remains independent of the axial coordinate [7, 15]. This is shown in Figure 1.2 for several different equivalence ratios of a lean H_2-air mixture. Cellular tubular flames offer structure similar to turbulent flames found in practical devices (local extinction and high local curvature), yet remain relatively simple (2D symmetric time independant structure).

The cellular instability forms predominately due to the thermal-diffusive properties of the mixture [5, 7]. This occurs for flames sustained in sub-unity Lewis number mixtures, and manifests as alternating patterns of reaction cells and extinction zones. The Lewis number (Le) is defined as the ratio of heat diffusivity of the mixture, over the mass diffusivity of the limiting reactant (fuel). The presence of convex (concave) curvature towards the fuel strengthens (weakens) mass flux, weakens (strengthens) heat loss, thereby enhancing (weakening) the flame. For strained flames, instabilities form along the direction of lesser

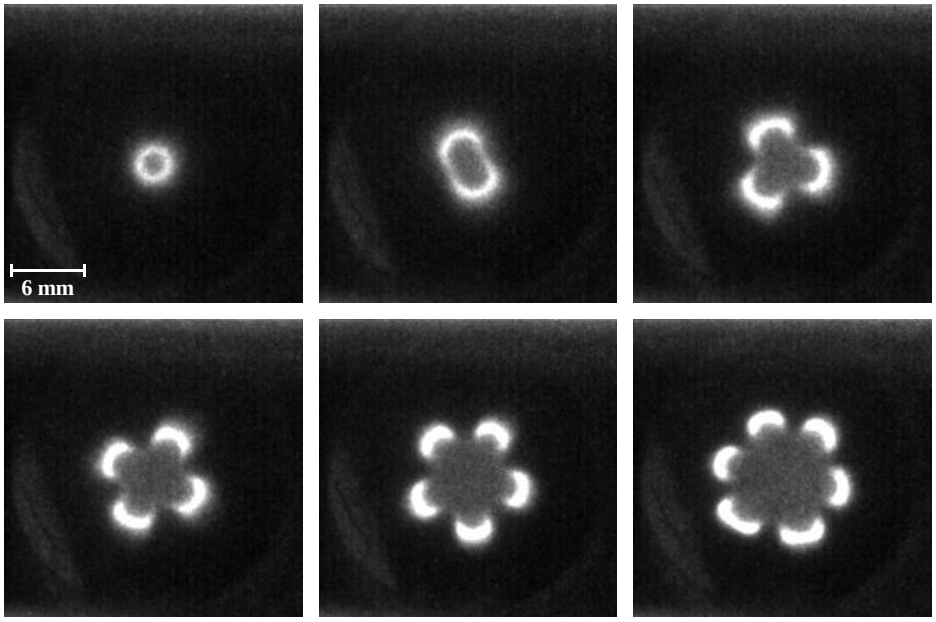

Figure 1.2 Chemiluminescence images of a N_2 dilution flame case showing the progression of cellular number by increasing the equivalence ratio

stretch [16], and cause the azimuthal pattern present in tubular flames [15].

For premixed tubular flames, cellular modes occur when the equivalence ratio is increased. This progression of cellular modes is shown in Figure 1.2 for a lean H_2-air mixture. As the flame is enriched, flame speed increases along with the flame tube radius. Once flame curvature decreases past a transition value [7], the flame surface becomes more stable in a cellular mode. The non-cellular tube breaks into individual cells with higher local curvature that stabilize at a larger radial coordinate with a higher flame speed. As the equivalence ratio increases further, more cells form to maximize local curvature. Note how the azimuthal symmetry can decrease for larger numbers of petals; here we will restrict our experimental investigations to flame cases with few numbers of cells that have good symmetry.

CHAPTER II

EXPERIMENTAL APPROACH

Experimental characterizations were performed with laser diagnostic techniques, which allow for quantitative, non-intrusive, and spatially resolved measurements of flame structure [17]. These types of measurements have not been previously performed in cellular flames, most likely due to the 3D and time dependent nature of most cellular flame geometries. Tubular cellular flames are ideal experimental targets for these types of detailed analyses, where they exhibit time-steady structure with 2D planar spatial dependency.

2.1 Tubular Burner

The tubular flame is sustained in the Vanderbilt tubular burner, which was previously designed and constructed to provide [18]: a laminar flow-field, uniform plug-flow velocity boundary conditions, and good optical access. A simplified schematic is shown in Figure 2.1. The flow domain is 8 mm in height and 24 mm in diameter, and there are 3 optical access windows oriented at 90° relative to each other. The flame is sustained around the burner axis, and exhausts both above and below the burner. Nitrogen co-flows are used to stabilize the flame and maintain a uniform inlet velocity profile and temperature.

The flame chemiluminescence was imaged using an ICCD camera (576×384, 5 ms gate) coupled to a multi-element UV lens (Nikon UV-Nikkor, f/4.5, 105 mm). A colored-glass filter (UG11) was used to discriminate the flame from ambient light and to selectively observe OH chemiluminescence (280-310 nm) [19]. The camera was focused at the center of the burner with a mirror oriented at 45°, to provide an axial image with the camera safely mounted out of the flame exhaust stream. In order to get an image with as shallow

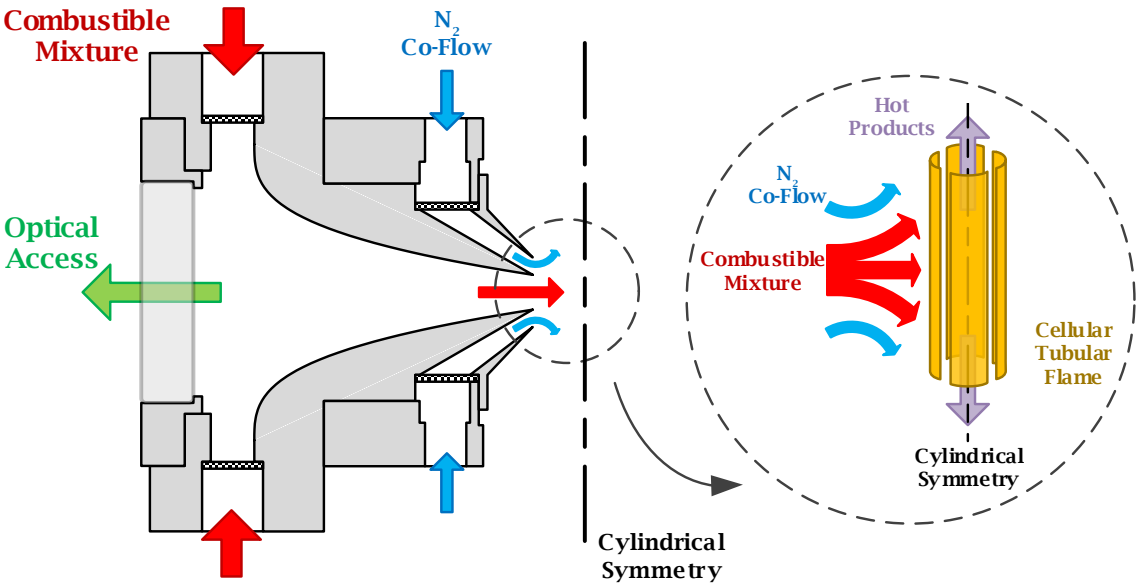

Figure 2.1 Simplified schematic of the premixed tubular burner.

of a depth of field as possible, the lens aperture was kept fully open. This imaging setup integrates chemiluminescence along the burner axis and records flame behavior outside of the burner; however, with the shallow depth of field the more intense signal is recorded at the focal plane located at the center of the burner.

While the cellular condition provides fixed rotational symmetry, there is no preferred angular orientation. The cellular patterns tend to rotate, maintaining uniform appearance and having no preference to rotation direction. Non-steady flames prohibit field measurements, thus a perturbation was introduced to provide a preferred flame orientation. A wire probe was inserted at the far edge of the burner, and the small hydrodynamic drag attracted a flame cell. The wire diameter (200 μm) and insertion length (∼3 mm into flow domain) were minimized to reduce the perturbation, while maintaining a stable flame orientation. Comparison of chemiluminescence images of the perturbed and non-perturbed cellular flames show the probe does not significantly alter the nature of the flame cells, and does not shift the symmetry axis from the burner axis.

2.2 Major Species and Temperature Measurement

Spontaneous Raman scattering was used to measure temperature and major species concentrations within the flame cases. The theoretical background for Raman scattering is complex and the detailed description is left to other texts (e.g. references [17,20]); included here for brevity is only a brief description. Raman scattering is the inelastic scattering of light from the electron cloud of a chemical species. The incident and scattered light differ by an energy "shift," due to loss (gain) of energy to (from) a molecular energy storage mode, and is termed Stokes (anti-Stokes) Raman scattering. As applied, only the stronger Raman signals are collected (Stokes), and only the transitions between vibrational levels are recorded [17]. The Raman signals contain a signature of the molecular content of the gas mixture; this allows the use of a single laser source to characterize the entire content of the gas mixture. The compromise of using spontaneous Raman scattering for gas phase measurements is that the signals are relatively weak, and only the major chemical species can be detected.

2.2.1 Experimental Setup

The simplified experimental schematic is shown in Figure 2.2, which was based on setups used successfully in prior investigations of non-cellular tubular flames [14,21]. The laser beam was generated by a Quanta Ray Lab-150 (532 nm, 9 ns pulse at 10 Hz), and was passed through a 3 stage pulse-stretcher [22] to decrease the peak pulse intensity. The average pulse energy delivered to the measurement zone ($\sim$130 mJ) was recorded for each measurement and used in the data-reduction procedure. The light beam was focused into the measurement zone with a 0.3 m focal length plano-convex lens, providing a nominal diameter of 180 μm through the measurement zone. The spatially resolved spectra were recorded along the laser line with a resolution of 86 μm. For convenience, the resolution of the traverse was set as 200 μm providing an overall grid resolution of 86×200 μm.

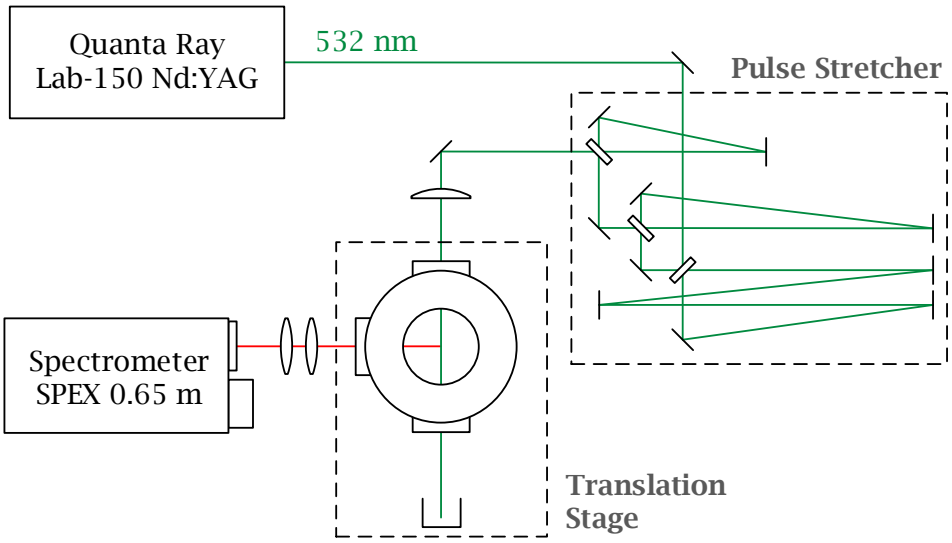

Figure 2.2 Simplified schematic of the Raman scattering laser light path.

To increase the signal, 600 laser shots were recorded during the LN/CCD exposure. A fast FLC shutter was used (∼45 μs opening time) to discriminate the Raman signal from background flame emission. The FLC shutter is partially transparent when closed, so a completely opaque mechanical shutter was also used (UniBLITZ, 6 ms opening time). Measurements were performed over a rectangular grid chosen *a priori* to capture a significant portion of the flame cellular structure. Due to symmetry, only the flame structure between the centers of one cell and the adjacent extinction zone are considered significant.

An uncertainty analysis was performed to estimate experimental error, and is included in Appendix A. The uncertainty present in the species and temperature measurements was found to increase monotonically with temperature. Characteristic values of temperature uncertainty in the experimental cases investigated are approximately ±70 K in the hot products and ±3 K in the room temperature reactants. Characteristic chemical species uncertainties are approximately ±2 % (mole fraction) in the hot products and ±0.5 % in the room temperature reactants.

2.2.1.1 Spectrometer

The spectrometer used during the course of this experimental investigation is a SPEX 0.75 m Czerny Turner Spectrometer that was previously modified [23] for an unrelated experimental campaign. The focusing mirror was replaced with one with a focal length of 0.65 m, which results in an approximate spectral range of 56 nm across the detector for the light frequencies of interest (532-700 nm) with the current diffraction grating (600 l/mm). To fully cover the Raman spectral range, two exposures must be taken at different grating angles. An alignment error is found in the rotation of the grating, manifesting as a spatial shift between the two spectrum images. The nature of this shift was not investigated in detail, and was corrected with calibration images prior to data reduction.

The absolute wavelength calibration of the spectrometer does not track directly with the mechanical odometer, due to the change in the focal length of the focusing mirror. To simplify use of the spectrometer, the relationship between the wavelength and odometer reading was determined using a calibration lamp (Hg-Ne Oriel Lamp). A second order polynomial fit was found to be sufficient,

$$\lambda \;=\; 4.7775 \cdot 10^{-4}\Lambda^2 + 1.5368\Lambda - 1348.4$$

where λ is the CCD chip center wavelength (nm) and Λ is the odometer reading (nm).

2.2.2 Data Reduction

Quantitative number densities of the major species N_j were determined with the experimental relation,

$$S_i = E \sum_j K_{ij} N_j \tag{2.1}$$

where S_i is the Raman signal, E is the total integrated laser pulse energy, K_{ij} is the temperature dependent calibration coefficient matrix, and the species considered are: CO_2, O_2, N_2, H_2O, and H_2. It is noted that this form is valid only for a fixed detection setup (which is commonly found experimentally); a more complete formulation is discussed elsewhere [17,24]. The gas temperature was inferred with the ideal gas law,

$$T = \frac{p_0}{k_b}\left(\sum_i N_i\right)^{-1} \tag{2.2}$$

where p_0 is the thermodynamic pressure and k_b is the Boltzmann constant. The spectra are composed of Raman "bands" of the rotational transitions for each molecule, which are integrated to obtain the Raman signals S_i. This is shown for example in Figure 2.3, where spectra are collected at multiple spatial locations along a line measurement.

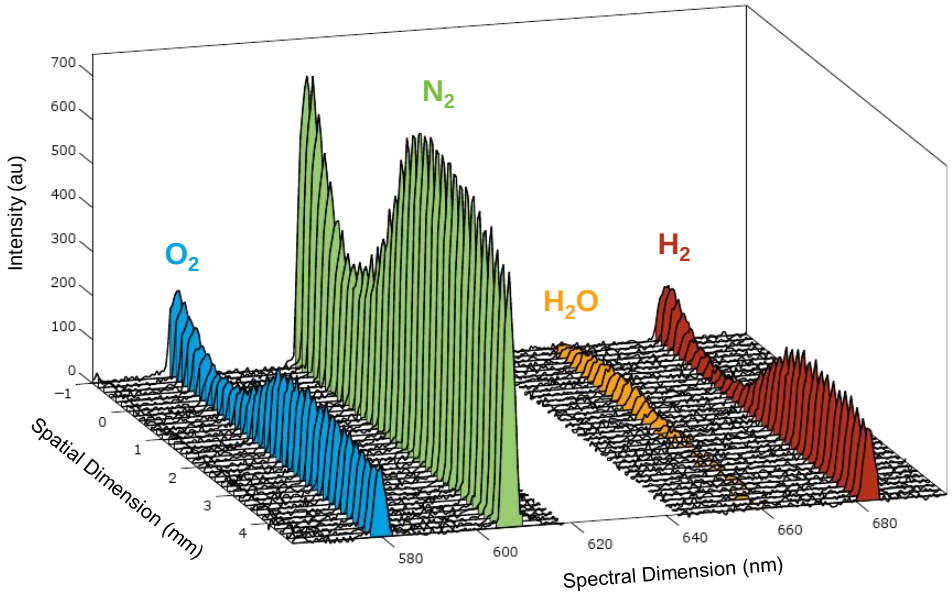

Figure 2.3 Example spectra of the Raman signal, showing the different bands for each major species.

The calibration matrix K_{ij} is sparse, and the non-zero entries were determined from theoretical Raman spectra simulated with `RAMSES` [25]. For the spectral bins used here, the sparsity is:

$$K = \begin{bmatrix} K_{CO_2,CO_2} & K_{CO_2,O_2} & 0 & 0 & K_{CO_2,H_2} \\ K_{O_2,CO_2} & K_{O_2,O_2} & 0 & 0 & K_{O_2,H_2} \\ 0 & 0 & K_{N_2,N_2} & 0 & 0 \\ 0 & 0 & 0 & K_{H_2O,H_2O} & K_{H_2O,H_2} \\ 0 & 0 & 0 & 0 & K_{H_2,H_2} \end{bmatrix}$$

The diagonal terms of the calibration matrix are the most significant and relate the Raman signal to the species number density. The off-diagonal terms are approximately an order of magnitude lower and relate the cross-talk of the different species on the others (e.g. K_{O_2,H_2} is the interference of the H_2 spectrum on the O_2 Raman signal).

The individual elements of the calibration matrix K_{ij} were determined over a temperature range (295-1800 K) using a Hencken burner (12.5 mm diameter) placed at the measurement location. Adiabatic equilibrium is assumed at the measurement location (15 mm from burner face), and the calculated species concentrations and temperature are used to generate the calibration matrix. Gas flow rates were controlled with flow controllers (Teledyne Hastings HFC-202/203), which are accurate to 1% full scale.

2.2.2.1 Background Subtraction

The images recorded by the LN/CCD detector contain both the Raman spectra and a background. The background is composed of multiple sources of different types: *repeatable* or *non-repeatable*, and *laser-based* or *non-laser-based*. The most difficult background effects to eliminate are *non-repeatable* and/or *laser-based*, since a direct background exposure (taken with the laser blocked) cannot be used for characterization. The dominant *non-repeatable* background is cosmic rays, which strike the CCD and appear as single pixels of

high signal. This issue is well mitigated in post-processing by removing sharp single-pixel features and replacing the missing points with an interpolated value [26]. Additionally, no *laser-based* background effects were found during the investigation of premixed tubular flames; significant effects were only found in the investigations of non-premixed tubular flames, which are not discussed here.

With a direct background characterization (where the laser is blocked for a LN/CCD exposure), the *repeatable* background may be simply subtracted. However, this results in the experiments taking twice as long. This method was used in previous investigations of non-cellular tubular flames [14], which extended the measurement from $\sim$4 to $\sim$8 minutes. For the cellular cases studied here, this approach would extend a $\sim$2 hour measurement to $\sim$4 hours and an alternative method was sought to reduce gas usage.

Upon examination of preliminary measurements, the *repeatable* background was observed to be spectrally diffuse. There is a large literature base for quantitative background post-processing techniques (e.g. see reference [27]), several methods of which are shown to work well for Raman data with spectrally diffuse backgrounds [28, 29]. The method implemented here is similar to that reported in literature, where the background is fit to each Raman spectrum using low-order polynomials with an iteratively-weighted least squares algorithm. The order of the polynomial (2-4) is chosen in situ during data reduction to satisfactorily handle the background. The same background subtraction parameters used for the cellular data sets were used on non-cellular validation data cases (shown in Figure 6 of reference [30]) to ensure confidence in the accuracy of the reported results. This background subtraction approach is well suited to the Raman spectra obtained in this work, where the good separation between Raman lines and the large areas of zero Raman signal (shown in Figure 2.3) increase the accuracy of the background estimation.

2.3 Hydroxyl Measurement

Laser induced fluorescence (LIF) was used to measure the minor species concentrations due to its high sensitivity and experimental simplicity [31]. Experimentally, LIF consists of two steps: energy absorption and photon emission. The excitation light source is tuned to excite an electronic transition, which then decays through radiative and non-radiative processes. The OH radical was detected using single-photon excitation of the $A^2\Sigma^+ \leftarrow X^2\Pi\ (1,0)\ Q_1(5)$ line (287.9 nm) followed by broadband detection of (0,0) and (1,1) fluorescence (300–340 nm). The dominant non-radiative process is collisional quenching, which is determined from a model [32] using the previously measured major species and temperature results.

2.3.1 Experimental Setup

A schematic of the experimental setup is shown in Figure 2.4. The laser system used was a Continuum ND6000 dye laser (laser dye: RD-590) pumped by a Quanta Ray Pro-350 Nd:YAG laser ($\sim$8 ns, 532 nm pulses at 10 Hz). The output of the dye laser was frequency-doubled to 287.9 nm. The laser light was formed into a sheet using a cylindrical lens (-100 mm focal length) followed by a spherical lens (300 mm). Radiation trapping was assumed to be negligible based on the observed linear dependence between florescence signal and laser excitation energy.

Variation of laser energy across the sheet was reduced by expanding the sheet width and using only the central portion of the beam. Span-wise laser sheet variation was recorded for each case by extinguishing the flame and imaging fluorescence off a target (white card) placed at the measurement zone, due to difficulties of obtaining a Rayleigh scattering image of the full sheet. This variation was found to be repeatable, and was processed consistently between the experimental cases and the calibration data sets.

The average laser-shot energy delivered to the burner ($\sim$4.2 mJ) was recorded for

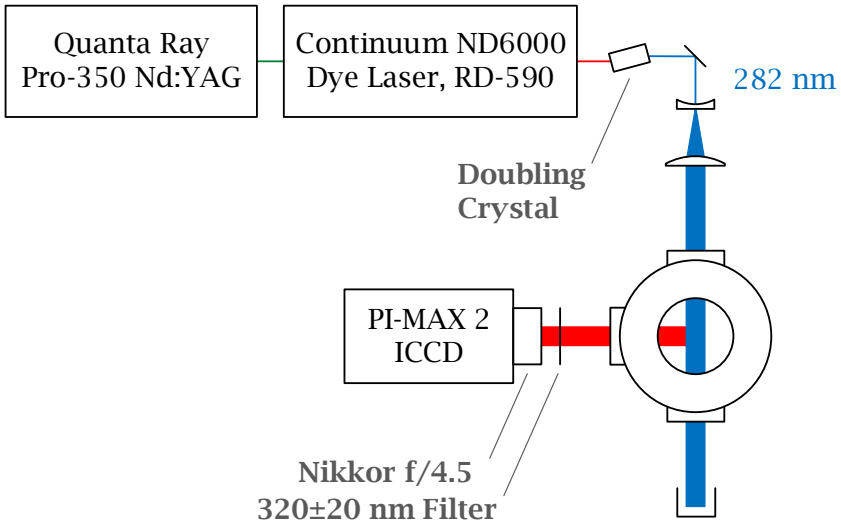

Figure 2.4 Simplified schematic of the planar LIF scattering laser light path.

each measurement and considered during the data-reduction procedure. Fluorescence was collected with a Nikon Nikkor f/4.5 lens coupled to a PI-MAX II ICCD camera. The flores-cence was imaged axially through a 45° mirror (Edmund Optics UV Enhanced Aluminum), resulting in an overall magnification of 1.14. A bandpass filter (Semrock FF01-320/40-50) combined with a 30-ns intensifier gate was used to reduce background flame emission. In each case, 300 laser shots were accumulated on-chip to increase the signal-to-noise ratio.

2.3.2 Data Reduction

Quantitative number densities were estimated using the standard quenching-corrected relation [17],

$$N_{OH} = \frac{C}{E}\left(\frac{A+Q}{A}\right)\frac{1}{f_b}S \approx \frac{C}{E}\frac{Q}{A}\frac{1}{f_b}S \tag{2.3}$$

where N_{OH} is the absolute number density of OH, C is a general calibration factor, E is the average laser-shot energy, A is the spontaneous transition rate, Q is the collisional-

quenching rate, f_b is the Boltzmann population fraction [33] for the ground state level $X^2\Pi$ $(\nu = 0)$ $(J = 5)$, and S is the collected signal (normalized by collection time). With the assumption that Q is much larger than A, the expression simplifies as shown. The effective Q is estimated as being equal to the $A^2\Sigma^+$ $(v = 0)$ quenching rate [32], and the effective A is lumped into the calibration factor.

Measurement uncertainty was estimated using the Kline-McClintock method [34] based on the terms in Equation 2.3. The absolute error is estimated as $\pm 2.0 \times 10^{15}$ cm^{-3} for OH over the experimental conditions investigated.

2.4 Atomic Hydrogen Measurement

Atomic hydrogen was detected using two photon LIF through $1 \rightarrow\rightarrow 3$ excitation (205.1 nm) followed by detection of the $2 \leftarrow 3$ fluorescence (656.5 nm). Two-photon absorption scales quadratically with laser fluence, hence using a short-pulse high-intensity scheme significantly reduces the relative probability of single-photon processes (e.g., major photolytic effects [35]) that scale linearly with laser fluence. It has been shown that using sub-picosecond pulse lengths decreased the relative effects of parasitic single-photon processes to negligible levels [36] for a rich premixed Bunsen flame.

2.4.1 Experimental Setup

A schematic of the experimental setup is shown in Figure 2.5. The laser system used was a Coherent Legend Elite Duo (100-fs pulses at 10 kHz), which was directly quadrupled using a fourth-harmonic generation unit [37]. The spectral profile was tuned to maximize fluorescence signal, resulting in a bandwidth of approximately 1 nm. Pulse spectral content and energy delivered to the measurement volume (4.30 ± 0.16 μJ) varied little over the course of the measurements and were considered constant during the data-reduction procedure. The beam diameter in the measurement volume was estimated at 400 μm, leading to a laser

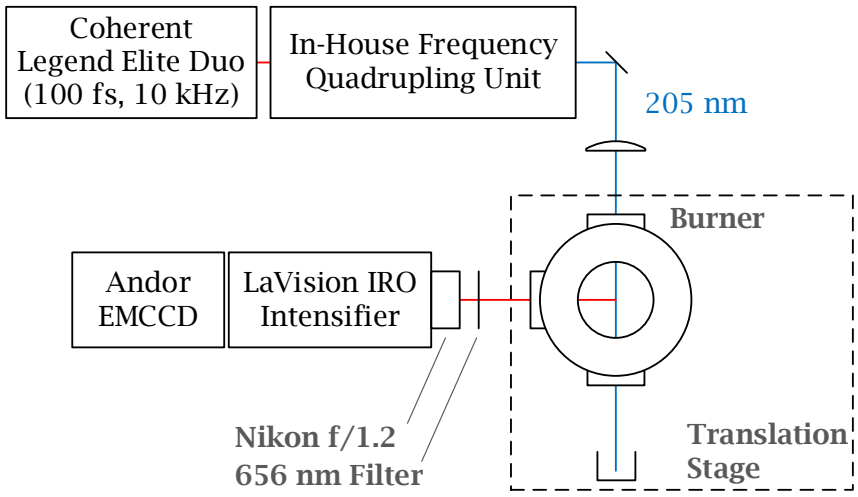

Figure 2.5 Simplified schematic of the two photon LIF atomic hydrogen experimental setup.

fluence of 3.4 mJ/cm^2; this laser fluence is below the laser-fluence threshold for photolytic production of H-atoms or stimulated-emission interference for H-atom LIF measurement with femtosecond lasers [36] and picosecond lasers [38].

Fluorescence was collected with a Nikon f/1.2 lens coupled to an intensified camera system, resulting in an overall magnification of 4.19. A bandpass filter (Semrock FF01-655/40-50) combined with a 300-ns intensifier gate was used to reduce background flame emission. The detection system was configured to maximize signal-to-noise, and consisted of a LaVision IRO intensifier and Andor Newton EMCCD detector. Despite optimization of detector alignment, the low optical magnification through the intensifier caused a significant instrument function that blurred the peaked spatial features being investigated. The instrument spatial response was estimated as a convolution [39] and was approximated from an acquired image of a knife edge. It was found to be well modeled as a Gaussian profile (full width at half maximum of 400 μm) within experimental error.

Measurement uncertainty was estimated using the Kline-McClintock method [34]

based on the terms in Equation 2.4. The absolute error is estimated as $\pm 1.3 \times 10^{15}$ cm^{-3} for H-atoms over the experimental conditions investigated. It is noted that the quantitative error associated with the quenching correction is not well known, as it was shown that using two different forms for quenching in non-cellular tubular flames resulted in differences significantly larger than the estimated measurement uncertainty [30].

2.4.2 Data Reduction

To facilitate comparison of the experimental and simulated number-density profiles, the instrument response was removed from the experimental data. Deconvolution was performed using two algorithms simultaneously to increase confidence in the processed results. The algorithms used were *Wiener* and *Lucy-Richardson* [40], implemented natively within the software package `MATLAB`. The differences between these two algorithms are expected to be small [40]; however, because of the presence of sharp peaks, the Wiener algorithm suffers from artificial oscillations (characteristic of Fourier Transform signal-processing methods). Both algorithms were found to be relatively insensitive to the deconvolution parameters, as long as the iteration count of the Lucy-Richardson algorithm was above a threshold (typically 3-4). Because there is good agreement of the local mean values between the two algorithms, the process of deconvolution is accepted as valid. Only data processed with the Lucy-Richardson algorithm are shown (using 6 iterations), because of the absence of artificial oscillations. The effect of the instrument function convolution is to systematically lower the peak value by approximately 20%, and is shown in Figure 2.6 for one non-cellular flame condition. Deconvoluted profiles of experimental data are shown with lines for clarity; unprocessed data are shown with symbols.

Quantitative number densities were estimated using the standard quenching-corrected

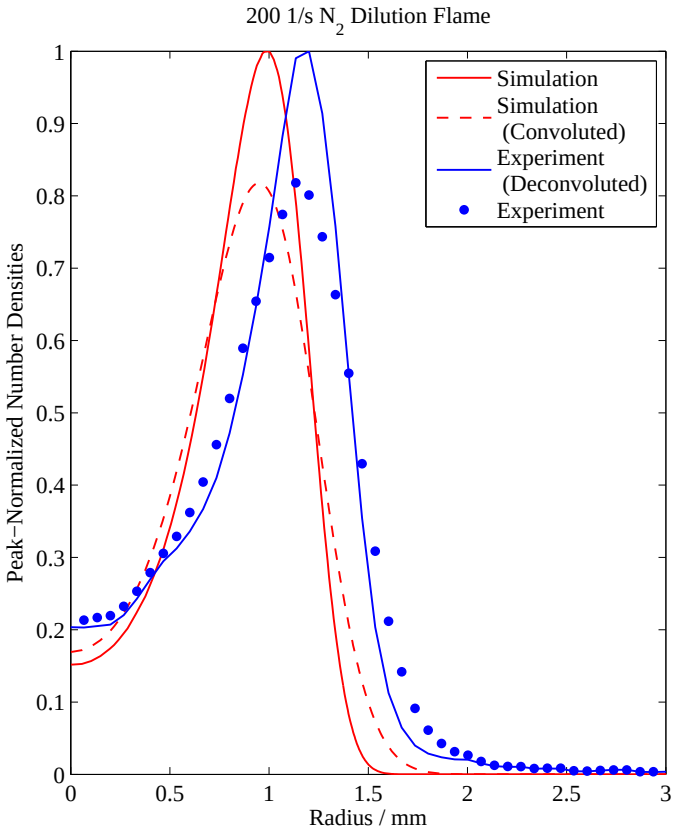

Figure 2.6 Comparison of H-atom data with and without the instrument function convolution. Scaling is preserved to show the effect of the convolution on the peak profile values.

relation,

$$N_H = C\left(\frac{A+Q}{A}\right)S \approx C\frac{Q}{A}S \tag{2.4}$$

where N_H is the absolute number density of hydrogen atoms, C is a general calibration factor, A is the spontaneous transition rate [41], Q is the estimated quenching rate, and S is the collected signal (normalized by collection time). Since Q is much larger than A, the expression simplifies as shown. Multiple laser shots were accumulated on-chip to increase signal-to-noise ($\sim 10^4$ shots), and multiple accumulations were taken (10) to estimate relative measurement uncertainty.

The quenching was calculated as done in [36, 38]:

$$Q = N_{tot}\sum_i x_i\sigma_i\nu_i = N_{tot}\sum_i x_i k_i \tag{2.5}$$

where N_{tot} is the total number density, x_i is the species mole fraction, σ_i is the temperature-dependent species quenching cross-section, and ν_i is the relative mean speed between the H-atoms and quencher. The species quenching rate is defined as $k_i = \sigma_i\nu_i$. For H-atom quenching, the value of k (cm^2/s) is found to be nearly constant for most of the quenching species except for H_2O, which seems to decrease with temperature [42]. The quenching rate Q was calculated using temperature-independent k_i [41] except for k_{H_2O}, where the quenchers considered are the major chemical species (H_2, H_2O, O_2, and N_2 or CO_2). The form of temperature dependence is taken as $T^{-0.5}$, and the methodology is discussed in more detail in [38].

The calibration factor was determined from predicted atomic-hydrogen number densities generated by a 12.5-mm Hencken burner at a position 20 mm downstream where the H-atom concentration is assumed to be in adiabatic equilibrium [43]. Figure 2.7a shows the LIF signal verses $N_H \times (A/Q)$ where N_H is predicted from adiabatic equilibrium. In these measurements, the flame background was substantial in the Hencken burner, and the

flame background was subtracted by recording camera images with and without the laser. However, there was still residual offset, as shown in Figure 2.7a. This offset was treated as residual flame background and subtracted from all of the measurements in the Hencken burner, which are shown in Figure 2.7b along with the computed equilibrium H-atom number densities. The slope of the linear fit in Figure 2.7a gives the calibration factor C in Equation 2.4. For the tubular-flame measurements, only the calibration constant is used to determine the H-atom concentrations measurements. The tubular flame has minimal flame background that is easily removed by measurements taken with and without the laser. For the tubular-flame cases, the LIF signal ahead of the flame front is zero within the estimated relative measurement uncertainty. The uncertainty bars shown in Figure 2.7 correspond to one standard deviation of the acquired signal. Because of increased signal at higher H-atom number densities, shorter integration times were used to prevent detector saturation; this had the unintended consequence of increasing the estimated measurement uncertainty.

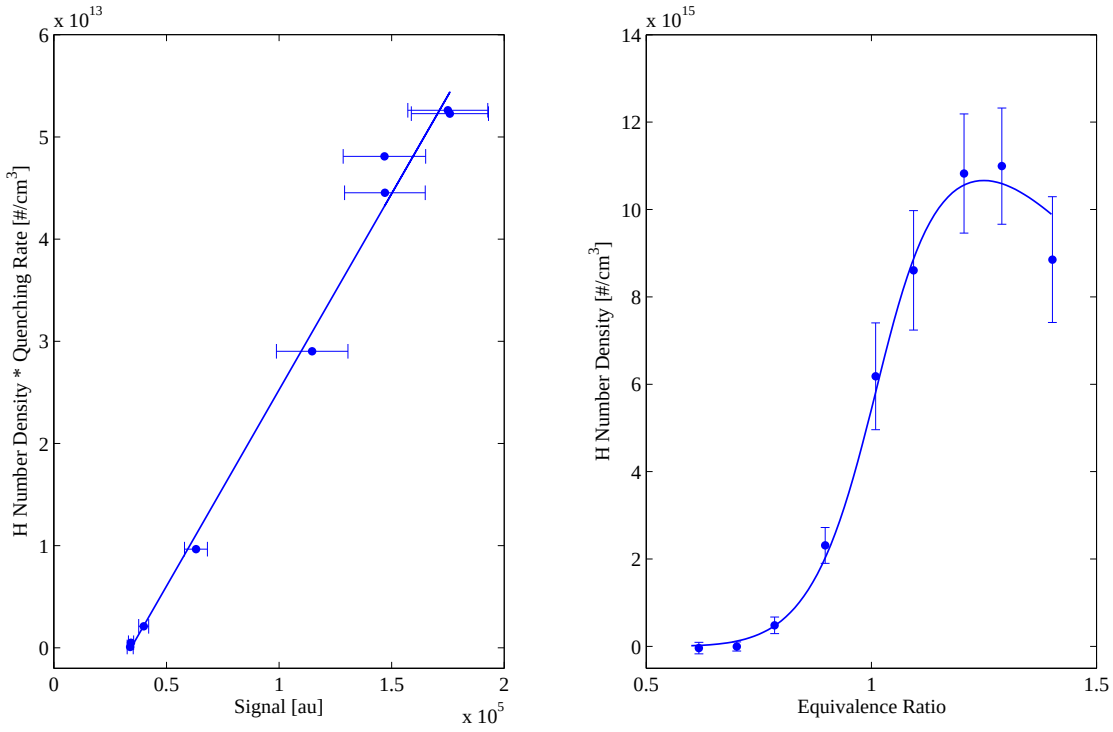

Figure 2.7 Calibration results for H-atom number density using a 12.5 mm diameter Hencken burner. Air flowrates were maintained at 9.0 slpm, and H_2 flowrates ranged from 2.3 to 5.3 slpm.

CHAPTER III

NUMERICAL APPROACH

The governing system of equations for multi-component reacting flow consist of conservation equations for momentum, chemical species, and internal energy. With the assumptions of negligible body force and viscous dissipation, the time dependent forms of these equations are expressed in *molecular flux* form [44] as,

$$0 = \frac{\partial}{\partial t}(\rho \boldsymbol{u}) + \nabla \cdot (\rho \boldsymbol{u}\boldsymbol{u}) + \nabla \cdot \boldsymbol{\sigma} \tag{3.1a}$$

$$m_i \omega_i = \frac{\partial}{\partial t}(\rho Y_i) + \nabla \cdot (\rho \boldsymbol{u} Y_i) + \nabla \cdot \boldsymbol{j}_i, \quad i \in \mathcal{S} \tag{3.1b}$$

$$Q = \frac{\partial}{\partial t}(\rho h) + \nabla \cdot (\rho \boldsymbol{u} h) + \nabla \cdot \boldsymbol{q} \tag{3.1c}$$

where ρ is the mass density, $\boldsymbol{u}$ is the velocity vector, $\boldsymbol{\sigma}$ is the stress tensor (also called the *molecular momentum-flux tensor* [44]), m_i is the molar mass of species i, ω_i is the production rate of species i, Y_i is the mass fraction of species i, $\boldsymbol{j}_i$ is the diffusive mass flux of species i, Q is radiative heat loss, h is the mixture enthalpy, $\mathbf{q}$ is diffusive heat flux, and $\mathcal{S}$ is the set of n species.

The equation set is commonly implemented in a more convenient form: the convective derivatives are expanded to reveal conservation of total mass, and the energy equation is expanded in terms of temperature.

$$0 = \frac{\partial}{\partial t}(\rho) + \nabla \cdot (\rho \boldsymbol{u}) \tag{3.2a}$$

$$0 = \rho \frac{\partial}{\partial t}(\boldsymbol{u}) + (\rho \boldsymbol{u} \cdot \nabla)\, \boldsymbol{u} + \nabla \cdot \boldsymbol{\sigma} \tag{3.2b}$$

$$m_i \omega_i = \rho \frac{\partial}{\partial t}(Y_i) + (\rho \boldsymbol{u} \cdot \nabla)\, Y_i + \nabla \cdot \boldsymbol{j}_i, \quad i \in \mathcal{S} \tag{3.2c}$$

$$Q = \rho c_p \frac{\partial}{\partial t}(T) + (\rho c_p \boldsymbol{u} \cdot \nabla) T + \nabla \cdot \left(\boldsymbol{q} - \sum_{j \in \mathcal{S}} h_j \boldsymbol{j}_j \right) + \\ + \left(\sum_{j \in \mathcal{S}} c_{pj} \boldsymbol{j}_j \right) \cdot \nabla T + \sum_{j \in \mathcal{S}} h_j m_j \omega_j \tag{3.2d}$$

where c_p is the specific heat of the mixture, h_j is the enthalpy of species i, and c_{pj} is the specific heat of species j. Note that in this form only $n-1$ species conservation equations (3.2c) are linearly independent with the conservation of total mass (3.2a). In practice it is convenient to replace one of species conservation equations (e.g. the main diluent species) with the mass-fraction constraint to enforce mass conservation [45]:

$$\sum_{i \in \mathcal{S}} Y_i = 1 \tag{3.3}$$

Historically, the implementation of custom combustion simulation codes is time consuming due to the large number of variable coefficients from chemical kinetics (ω_i), thermodynamics (c_p, c_{pj} h_j), and diffusive transport terms (μ, $\mathcal{D}_{ij}$, $\mathcal{D}_i^T$, λ). Software libraries have been developed by the community that calculate these coefficients (e.g. `EGLIB` [46], `CHEMKIN` [47, 48], `Cantera` [49]) and are available for implementation into custom codes. This greatly reduces the difficulty of creating a custom simulation code. The mathematical form of these coefficients is not included here for brevity, but may be found in many chemical engineering and combustion textbooks (e.g. see references [45, 50, 51]).

The species reaction rates are calculated with a detailed chemical kinetic mechanism to simulate the full physics of the chemical reaction. `CHEMKIN` [47] is used to compute the species net production rates (ω_i) and the thermodynamic terms (c_p, c_{pj} h_j). The mechanism used for hydrogen combustion [52] consists of 19 reactions, 3 major species (H_2, O_2, H_2O), 5 minor species (H, O, OH, HO_2, H_2O_2), and 1 non-reacting species (N_2). A carbon-containing sub-mechanism [53] consisting of an additional 14 reactions, 1 major species (CO_2), and 2 minor species (CO, HCO) was added to allow reactivity of CO_2.

3.1 Diffusive Transport

The stress tensor ($\boldsymbol{\sigma}$), diffusive mass flux ($\boldsymbol{j}_i$), and diffusive heat flux ($\boldsymbol{q}$) are defined in terms of transport coefficients and spatial gradients [44, 45, 54],

$$\boldsymbol{\sigma} = -\mu\left[\nabla\boldsymbol{u} + (\nabla\boldsymbol{u})^\top\right] + \left[p - \left(\kappa - \tfrac{2}{3}\mu\right)(\nabla\cdot\boldsymbol{u})\right]\boldsymbol{\delta} \tag{3.4a}$$

$$\boldsymbol{j}_i = \rho Y_i \boldsymbol{u}_i^d = -\sum_{j\in\mathcal{S}} Y_i \mathcal{D}_{ij}\nabla x_j - Y_i\mathcal{D}_i^T\nabla\ln T, \quad i\in\mathcal{S} \tag{3.4b}$$

$$\boldsymbol{q} = \sum_{i\in\mathcal{S}} h_i\rho Y_i\boldsymbol{u}_i^d - \lambda\nabla T + \boldsymbol{q}^D \tag{3.4c}$$

where μ is the dynamic viscosity, p is the pressure, κ is the dilational viscosity, $\boldsymbol{u}_i^d$ is the diffusion velocity of species i, $\mathcal{D}_{ij}$ is the mass diffusion matrix, x_j is the mole fraction of species j, $\mathcal{D}_i^T$ is the thermal diffusion coefficient, λ is the heat conductivity, and $\boldsymbol{q}^D$ is the Dufour effect. Pressure diffusion is neglected due to the low flow acceleration (e.g. see reference [55]).

The last terms in Equations 3.4b and 3.4c commonly referred to as *thermal diffusion*. These two terms are comprised of the Soret ($Y_i\mathcal{D}_i^T\nabla\ln T$) and Dufour ($\boldsymbol{q}^D$) effects. The Soret effect is the interaction of temperature gradients on mass flux, and the Dufour effect is the interaction of concentration gradients on heat flux. It has been shown for hydrogen combustion that the Soret effect is important for predicting accurate flame structure, while the Dufour effect is negligible [56, 57].

Due to the low flow velocities, the low-Mach number assumption [45] is valid and may be applied to reduce the coupling between the energy and momentum fluxes. This splits the pressure into two terms: $p = p_0 + p_1$. The scalar thermodynamic pressure p_0 is used with the ideal gas constitutive equation,

$$p_0 = \rho RT\sum_{i\in\mathcal{S}}\frac{Y_i}{m_i} \tag{3.5}$$

and the perturbed pressure p_1 is a field variable that only appears in the stress tensor $\boldsymbol{\sigma}$. It is

advantageous to define a "lumped perturbed pressure" $\widetilde{p}_1$ that includes the dilational strain term in the stress tensor [45, 58],

$$\widetilde{p}_1 = p_1 - \left(\kappa - \tfrac{2}{3}\mu\right)(\nabla \cdot \boldsymbol{u}) \tag{3.6}$$

This allows the stress tensor to be expressed without evaluating dilational viscosity κ,

$$\boldsymbol{\sigma} = -\mu\left[\nabla \boldsymbol{u} + (\nabla \boldsymbol{u})^\top\right] + (p_0 + \widetilde{p}_1)\,\boldsymbol{\delta}$$

which many transport libraries do not implement (e.g. `CHEMKIN` [48] or `Cantera` [49]).

Local mass conservation is enforced in Equation 3.4b when using an approximate transport formulation by introducing a species-independent spatially-varying correction velocity [4]. This is applied both before and after adding the Soret contribution to enforce the two conservation constraints [45]:

$$\sum_{i\in\mathcal{S}} Y_i \mathcal{D}_{ij} = 0, \quad j \in \mathcal{S} \tag{3.7a}$$

$$\sum_{i\in\mathcal{S}} Y_i \mathcal{D}_i^T = 0 \tag{3.7b}$$

With all these assumptions, the diffusive flux terms simplify to:

$$\boldsymbol{\sigma} = -\mu\left[\nabla \boldsymbol{u} + (\nabla \boldsymbol{u})^\top\right] + (p_0 + \widetilde{p}_1)\,\boldsymbol{\delta} \tag{3.8a}$$

$$\rho Y_i \boldsymbol{u}_i^d = -\sum_{j\in\mathcal{S}} Y_i \mathcal{D}_{ij} \nabla x_j - Y_i \mathcal{D}_i^T \nabla \ln T, \quad i \in \mathcal{S} \tag{3.8b}$$

$$\boldsymbol{q} = \sum_{i\in\mathcal{S}} h_i \rho Y_i \boldsymbol{u}_i^d - \lambda \nabla T + \boldsymbol{q}^D \tag{3.8c}$$

3.1.1 Multicomponent Form

The physically accurate form of the transport coefficients ($\mathcal{D}_{ij}$, $\mathcal{D}_i^T$, μ, λ) is the multicomponent form. These coefficients are computationally expensive to calculate for gas mixtures due to the need to perform a matrix inversion to determine each coefficient. These matrices (transport linear systems [44, 59, 60]) each have sizes on the order of the number of chemical species, which can be large for practical combustion mixtures. Legacy software libraries (e.g. `CHEMKIN` [48], `Cantera` [49]) use direct inversion and require O(n^3) operations per matrix, where n is the size of the matrix. More recent advances in iterative techniques provide speedup [60], and the highly optimized library `EGLIB` [46] calculates the coefficients with O(n^2) operations.

The specific form of the mass diffusion matrix ($\mathcal{D}_{ij}$) and thermal diffusion ($\mathcal{D}_i^T$, $\boldsymbol{q}^D$) differ depending on the software library. `EGLIB` [46] calculates diffusive transport in terms of the computational variables ($\widetilde{\mathcal{D}}_{ij}$,$\widetilde{\chi}_i$):

$$Y_i\mathcal{D}_{ij} = \rho\widetilde{\mathcal{D}}_{ij} \tag{3.9a}$$

$$Y_i\mathcal{D}_i^T = \rho\sum_{j\in\mathcal{S}}\widetilde{\mathcal{D}}_{ij}\widetilde{\chi}_j x_j \tag{3.9b}$$

$$\boldsymbol{q}^D = p_0\sum_{i\in\mathcal{S}}\frac{m}{m_i}\widetilde{\chi}_i Y_i \boldsymbol{u}_i^d \tag{3.9c}$$

`CHEMKIN` [48] calculates diffusive transport in terms of the computational variables ($\widetilde{\mathcal{D}}_{ij}$, $\widetilde{\mathcal{D}}_i^T$):

$$Y_i\mathcal{D}_{ij} = \rho\frac{m_i m_j}{m^2}\widetilde{\mathcal{D}}_{ij} \tag{3.10a}$$

$$Y_i\mathcal{D}_i^T = \widetilde{\mathcal{D}}_i^T \tag{3.10b}$$

$$\boldsymbol{q}^D = p_0\sum_{i\in\mathcal{S}}\frac{\widetilde{\mathcal{D}}_i^T}{\rho Y_i}\nabla x_i \tag{3.10c}$$

3.1.2 Mixture Average Form

Calculation of the transport coefficients for practical simulation conditions commonly rely on approximations to reduce numerical expense. The mixture averaged approximation [3] allows the calculation of each transport coefficient with O(n) operations. `CHEMKIN` [48] is used to calculate the approximations, which are expressed in terms of the computational variables ($\widetilde{\mathcal{D}}_i$,$\widetilde{\chi}_i$),

$$Y_i \mathcal{D}_{ij} = \begin{cases} \frac{m_i}{m} \rho \widetilde{\mathcal{D}}_i, & i = j \\ 0, & i \neq j \end{cases} \tag{3.11a}$$

$$Y_i \mathcal{D}_i^T = -\frac{m_i}{m} \rho \widetilde{\mathcal{D}}_i \widetilde{\chi}_i, \quad m_i < 5 \tag{3.11b}$$

$$\boldsymbol{q}^D = \mathbf{0} \tag{3.11c}$$

It is noted that the approximation for thermal diffusion ($\widetilde{\chi}_i$) provided by `CHEMKIN` is semi-empirical and doesn't appear to be widely accepted by the simulation community. Even the documentation states that the form is "considerably less accurate than the thermal diffusion coefficients that are computed from the multicomponent formulation" [48].

3.2 Boundary Layer Assumption

Under the boundary layer assumption for a stagnation point flow field [11], strong unidirectional flow divergence decouples the scalar and velocity fields from the direction of flow divergence. The detailed derivation of the tubular flame structure is discussed elsewhere [6, 15], but the salient results are as follows: the axial flow divergence allows the velocity field to be expressed in terms of a linear axial velocity gradient W,

$$\boldsymbol{u} = u\left(r,\theta\right) \hat{\boldsymbol{r}} + v\left(r,\theta\right) \hat{\boldsymbol{\theta}} + zW\left(r,\theta\right) \hat{\boldsymbol{z}} \tag{3.12}$$

the scalar fields (Y_i and T) are not dependent on z, and the axial dependance of the perturbed pressure field $\widetilde{p}_1$ is expressed as a scalar pressure eigenvalue H,

$$H = \frac{1}{z}\frac{\partial \widetilde{p}_1}{\partial z} \tag{3.13}$$

This is the same fundamental assumption used to express axially-opposed jet flames as 1D [61], where instead the radial divergence creates a radial pressure eigenvalue and a radially-uniform flame structure.

Stagnation flow fields have been widely used in combustion and chemical-engineering applications, though more commonly in the axially-opposed jet orientation [61]. The advantage of using the tubular orientation lies in the curvature of the flow field—this creates a uniformly curved and stretched non-cellular flame, and this aspect causes cellular flames to have 2D planar spatial dependency (r, θ).

The accuracy of the boundary layer assumption has recently been investigated for the axial opposed jet [62–65]. The works all draw similar conclusions: the boundary-layer approximation is valid for a given burner design over a range of flow velocities. This type of analysis appears to be largely absent from the tubular burner literature, with the exception of one experimental investigation that confirmed the axial independence of W for the given flow velocity and burner geometry [66].

3.3 Governing Equations

The form of the governing equations is similar to the previous non-cellular tubular flame work [67, 68] with the relaxation of full azimuthal symmetry. A strong distinction is that none of the 1D non-cellular tubular flame codes resolve the perturbed pressure field $\widetilde{p}_1$. In the 2D cellular formulation this variable must be resolved in order to resolve all components of the velocity field. The functional dependance of the perturbed pressure field

is found from integration of Equation 3.13,

$$\widetilde{p}_1 = \frac{z^2}{2} H + I\left(r, \theta\right) \tag{3.14}$$

where I is the radial and tangential pressure dependance. With this, the problem is formulated in differential form in terms of the primitive variables (u, $\frac{v}{r}$, W, H, I, T, Y_i), and the governing equations are as follows: conservation of total mass,

$$0 = \frac{\partial}{\partial r}\left(r\rho u\right) + \frac{\partial}{\partial \theta}\left(\rho v\right) + r\rho W \tag{3.15}$$

conservation of momentum in the radial direction,

$$\begin{aligned} 0 = {} & \rho\left(u\frac{\partial u}{\partial r} + \frac{v}{r}\frac{\partial u}{\partial \theta} - \frac{v^2}{r}\right) + \frac{\partial I}{\partial r} - \frac{1}{r}\frac{\partial}{\partial r}\left(2\mu r\frac{\partial u}{\partial r}\right) \\ & - \frac{1}{r}\frac{\partial}{\partial \theta}\left[\mu\left(r\frac{\partial}{\partial r}\left(\frac{v}{r}\right) + \frac{1}{r}\frac{\partial u}{\partial \theta}\right)\right] - \mu\frac{\partial W}{\partial r} + \frac{2\mu}{r}\left(\frac{1}{r}\frac{\partial v}{\partial \theta} + \frac{u}{r}\right) \end{aligned} \tag{3.16}$$

conservation of momentum in the azimuthal direction,

$$\begin{aligned} 0 = {} & \rho\left(u\frac{\partial v}{\partial r} + \frac{v}{r}\frac{\partial v}{\partial \theta} + \frac{uv}{r}\right) + \frac{1}{r}\frac{\partial I}{\partial \theta} - \frac{1}{r^2}\frac{\partial}{\partial r}\left[\mu r^2\left(r\frac{\partial}{\partial r}\left(\frac{v}{r}\right) + \frac{1}{r}\frac{\partial u}{\partial \theta}\right)\right] \\ & - \frac{1}{r}\frac{\partial}{\partial \theta}\left[2\mu\left(\frac{1}{r}\frac{\partial v}{\partial \theta} + \frac{u}{r}\right)\right] - \frac{\mu}{r}\frac{\partial W}{\partial \theta} \end{aligned} \tag{3.17}$$

conservation of momentum in the axial direction,

$$0 = \rho\left(u\frac{\partial W}{\partial r} + \frac{v}{r}\frac{\partial W}{\partial \theta} + W^2\right) + H - \frac{1}{r}\frac{\partial}{\partial r}\left(\mu r\frac{\partial W}{\partial r}\right) - \frac{1}{r}\frac{\partial}{\partial \theta}\left(\frac{\mu}{r}\frac{\partial W}{\partial \theta}\right) \tag{3.18}$$

conservation of energy,

$$0 = \rho\left(u\frac{\partial T}{\partial r} + \frac{v}{r}\frac{\partial T}{\partial \theta}\right) + \frac{1}{rc_p}\frac{\partial}{\partial r}\left(rq_r - r\sum_{i\in\mathcal{S}} h_i\rho Y_i u_i^d\right) + \frac{1}{rc_p}\frac{\partial}{\partial \theta}\left(q_\theta - \sum_{i\in\mathcal{S}} h_i\rho Y_i v_i^d\right)$$

$$+\frac{1}{c_p}\sum_{i\in\mathcal{S}}\left(\rho Y_i u_i^d c_{pi}\frac{\partial T}{\partial r}+\rho Y_i v_i^d c_{pi}\frac{1}{r}\frac{\partial T}{\partial \theta}\right)+\frac{1}{c_p}\sum_{i\in\mathcal{S}}\left(\omega_i h_i m_i\right)+\frac{Q}{c_p} \tag{3.19}$$

and conservation of species,

$$0=\rho\left(u\frac{\partial Y_i}{\partial r}+\frac{v}{r}\frac{\partial Y_i}{\partial \theta}\right)+\frac{1}{r}\frac{\partial}{\partial r}\left(r\rho u_i^d Y_i\right)+\frac{1}{r}\frac{\partial}{\partial \theta}\left(\rho v_i^d Y_i\right)-\omega_i m_i,\quad i\in\mathcal{S} \tag{3.20}$$

The pressure eigenvalue H is discretized over the domain and treated implicitly to allow the velocity boundary conditions to be specified [68]. The following equation is added to the equation set,

$$0=\frac{\partial H}{\partial r} \tag{3.21}$$

with the boundary condition,

$$0=\frac{\partial H}{\partial \theta} \tag{3.22}$$

This additional equation is required to enforce a uniform value for the H "eigenvalue," while keeping the velocity boundary conditions from over specifying the problem [68].

Radiation heat loss Q is included in the optically-thin form [69],

$$Q=4\sigma\left(T^4-T_b^4\right)p_0\sum_i\left(x_i a_i\right),\quad i\in\{\mathrm{H_2O},\mathrm{CO_2}\} \tag{3.23}$$

where σ is the Stefan-Boltzmann constant, T_b is the background temperature, and a_i is the Planck mean absorption coefficient of species i (given in [69]).

3.3.1 Boundary Conditions

The computational domain consists either of a full 2D polar domain ($r\in[0,R]$, $\theta\in[0,2\pi]$) or an angular section ($r\in[0,R]$, $\theta\in\left[0,\frac{2\pi}{N}\right]$) to force N-fold cellular symmetry.

The azimuthal bounds have symmetry conditions for all variables except azimuthal velocity v, which is set to zero at $\theta = 0$. This condition is needed for a time-steady solution to keep the flame from arbitrarily rotating in the domain. For the symmetric cellular cases studied here, this velocity azimuthal boundary condition is natural and is observed along the centers of each cell and extinction zone.

The radial boundary conditions are: inflow at the outer nozzle ($r = R$),

$$u = u_{BC}, \qquad \frac{v}{r} = 0, \qquad W = W_{BC}, \qquad Y_i(u + u_i^d) = (Y_i u)_{BC}\,, \qquad T = T_{BC}$$

and centerline conditions at the origin ($r = 0$),

$$u = 0, \qquad \frac{v}{r} = 0, \qquad \frac{\partial W}{\partial r} = 0, \qquad \frac{\partial Y_i}{\partial r} = 0, \qquad \frac{\partial T}{\partial r} = 0, \qquad I = 0$$

It is noted that the boundary condition for the absolute value of pressure I is arbitrary, as only spatial gradients appear in the momentum conservation equations.

The centerline conditions are required to remove the singularity at the origin which occurs when using polar coordinates for a full domain solution. The form of the boundary conditions is consistent with previous 1D simulations [67, 68], and is accurate for partial-domain solutions. For full domain solutions this boundary condition is inaccurate for non-symmetric flame orientations, as the flame center is artificially fixed at the origin. Thus we restrict our study to only symmetric flame orientations, which are fortuitously observed for the experimental cases.

3.3.2 Staggered Mesh

The primitive variable formulation of the governing conservation equations can be difficult to solve due to numerical oscillations [70, 71] stemming from central difference stencils used on the first derivative terms in the mass and momentum conservation equations.

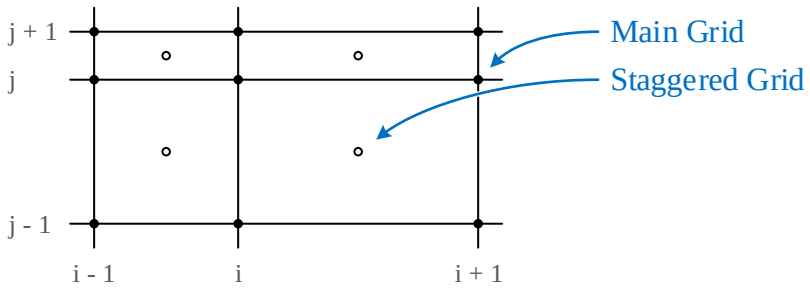

Figure 3.1 Schematic of the main and staggered grid structures used to suppress numerical oscillations.

The oscillatory behavior may be suppressed by resolving specific variables and equations on a secondary staggered grid, which converts first-derivative stencils from oscillatory three-point central difference versions to non-oscillatory versions.

The definition of the staggered grid used here is shown schematically in Figure 3.1, where the staggered grid is shifted from the main grid along both coordinate directions. It is noted that this grid definition differs from that reported in [70, 71] but is similar to the definition used in `OPPDIF` [61]. Only one variable (I) and only one equation (3.15) are resolved on the staggered grid.

3.4 Solution Method

The governing equations are discretized with finite differences [72] over a non-uniformly spaced tensor-product grid in polar coordinates. First-order upwind differencing is used on radial convective terms and second-order central differencing is used for all other derivatives, resulting in a 9 point box stencil. Adaptive mesh refinement is implemented in the radial direction by the method discussed in [73], where local grid spacing is subdivided to increase resolution through the flame front. The variation of grid spacing in the azimuthal direction was found to be unimportant, and equispaced nodes are used for sim-

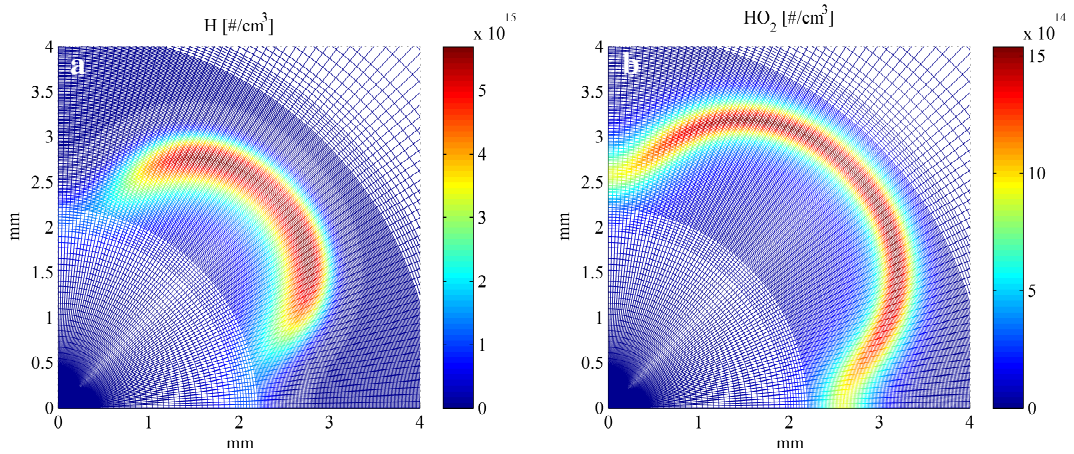

Figure 3.2 The tensor product grid with adaptive refinement is successful at capturing cellular flame structure, despite the inefficient node placement at the coordinate origin. Shown is the same grid twice with two important minor species: H (a) and HO_2 (b).

plicity. Grid independence is confirmed by comparing converged solutions on successively refined grids, and all solutions reported here correspond to the final highest-resolution grid. The final grid for a 4-cell flame case is shown in Figure 3.2, and is shown twice with different minor species to illustrate how well the adaptive grid refinement captures the flame structure.

It is noted that the use of a tensor-product mesh [74] in polar coordinates suffers from inefficient node placement near the coordinate origin (shown in Figure 3.2), where the physical spacing between nodes converges to zero in the azimuthal direction. More efficient techniques are discussed in literature (e.g. block-based [75] or cell-based [74]); however, a tensor-product mesh is substantially simpler to implement and the low complexity of the flame structure affords use of less efficient meshing and solution strategies (e.g. see discussion in [74]).

The governing system of equations is solved using mesh-sequencing and pseudo-transient continuation [76–78], where the final converged solution is reported in fully implicit form. During development it was found that good convergence could be achieved by

appending a pseudo-transient term simply on the energy equation. The solution algorithm is a Newton search with left-preconditioning (restricted additive Schwarz [79] solved exactly with 1 node overlap). The Jacobian and the preconditioner are formed intermittently during the solution process, and refreshing the matrices every 5 Newton steps provided a good tradeoff between computational speed and convergence. The local linear problem is solved with GMRES, and the final solution is reported with a 2-norm error tolerance of 10^{-4}.

The computational requirements for the 2D simulations of cellular tubular flames are modest. Partial domain solutions ($\theta \in \left[0, \frac{2\pi}{N}\right]$) were capable of being solved on a single PC (2.66 GHz Intel Xeon W3520, 4 cores, 10 GB RAM); however, most cases were solved using a small cluster (5 Xeon W3520 PC's, 20 cores, 50 GB total RAM, Gigabit Ethernet interconnect) for speed-up. The maximum number of cores used for simulations was 19, leaving 1 core for data analysis and the graphical user interface. The additional memory present in the cluster was required for the full domain solutions ($\theta \in [0, 2\pi]$).

3.5 Software Design

The numerical simulation is implemented with `PETSc` [80], which provides a variety of solution algorithms, data structures, and simplified interfaces to parallel communication tasks. The code is written predominantly in C++, with sections of Fortran and C to provide interfaces to the Fortran libraries `CHEMKIN II` [47, 48] and `EGLIB` [46]. The program design follows the standard parallel programming paradigm: a single process runs on each computer core, all operate with a single shared data set, and communication is handled with a message passing interface (`MPICH`). The overall program design is shown in Figure 3.3 as a flowchart.

Parallelization is achieved by partitioning the spatial domain into sections and distributing variables over each section to a separate process. The computational efficiency is known to be strongly sensitive to the partitioning strategy (e.g. see discussion in [81]).

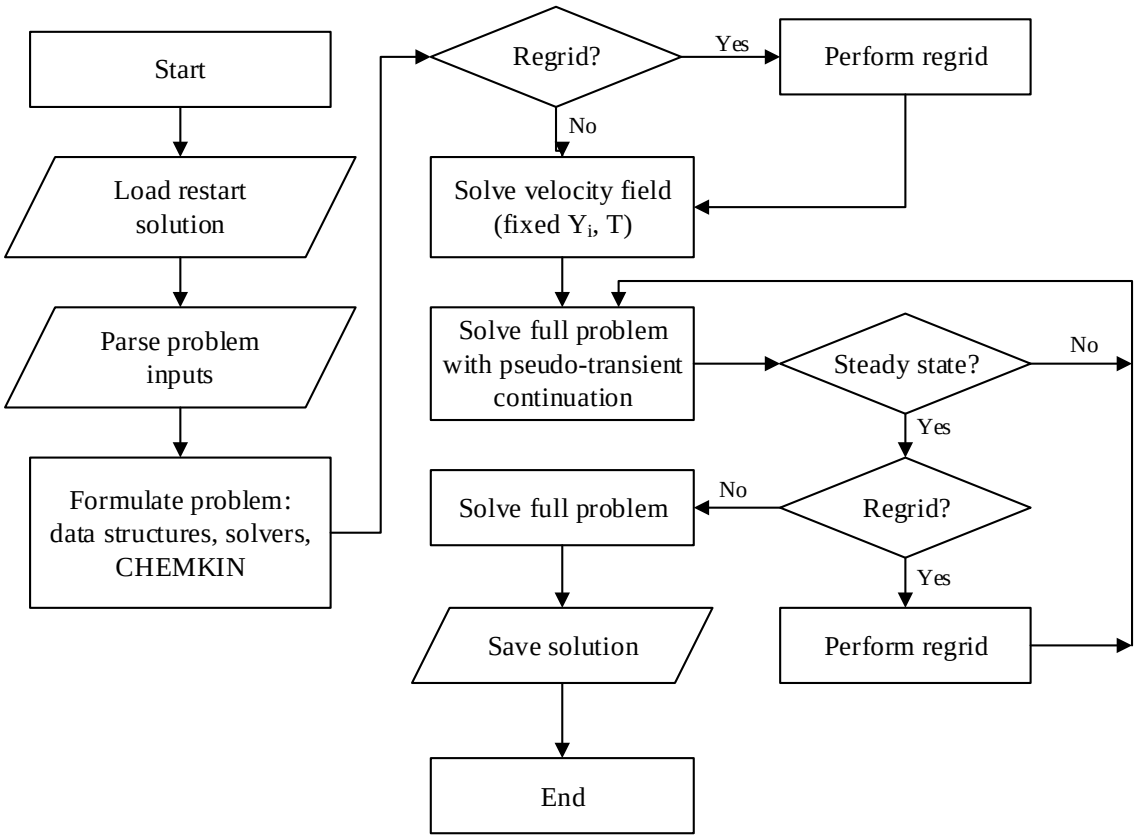

Figure 3.3 Flowchart of the numerical simulation software used for all PETSc-based codes developed in this work.

During development it was found that simply partitioning the domain along the angular direction to form radial "strips" provided satisfactory convergence. The computational efficiency of this domain decomposition strategy is shown in Figure 3.4 for a test problem solved across increasing numbers of cores (72×237 grid points, 4 cell N_2 flame case, single pseudo-transient solve to an error tolerance of 10^{-2}). The parallel efficiency is defined as [81],

$$\eta\left(n\right) = \frac{t_1}{n\, t_n} \tag{3.24}$$

where t_1 is the wall-clock simulation time for execution across 1 core, and t_n is the wall-clock time for execution across n cores. The parallel efficiency peaks at at approximately 60% for the test problem. This isn't as efficient as more optimized approaches (e.g. $>$70% [81]) but for the relatively low complexity of cellular tubular flames this was found to be sufficient: grid-independent results can be achieved with multicomponent properties and detailed chemistry in usually $<$8 hours of compute time across 19 cores of the 5 PC cluster.

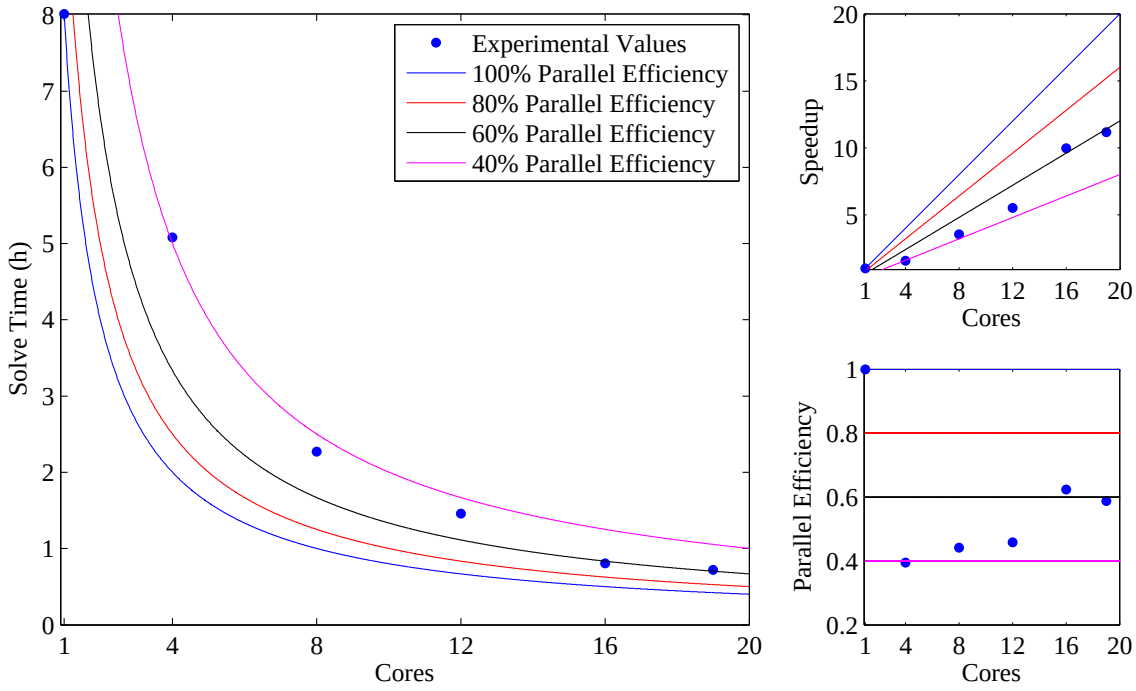

Figure 3.4 Parallel efficiency of a test problem solved across an increasing number of cores (72×237 grid points, 4 cell N_2 flame case, single pseudo-transient solve to an error tolerance of 10^{-2}).

CHAPTER IV

CASE STUDIES

Tubular flame cases were examined experimentally and numerically with a short parametric study in stretch (200 s^{-1} or 400 s^{-1}) and dilution (N_2 or CO_2) to broadly characterize the cellular structure. The number of cells was chosen with the equivalence ratio [7]: a 4 cell state for low stretch cases, which resulted in 3 cells for high stretch cases. The size of this study was kept low (4 flame cases total) to mitigate the amount of time spent on data collection and numerical simulation in favor of analysis on the cellular flame structure. Cellular tubular flames have not been examined before with detailed experimental or numerical approaches, and the potential range of non-trivial test cases is large [7]: covering up to $\sim$8 cells, additional diluent gas types, and non-symmetric flame cases. With the results from this brief case study, additional experimental campaigns may be planned with more specificity and executed in the future.

Chemiluminescence images of the cellular cases are shown in Figure 4.1, and values for the boundary conditions are included in Table 4.1. The value for the axial velocity gradient boundary condition W_{BC} is difficult to quantify and was not experimentally measured. For stagnation burners with contoured nozzles, W_{BC} is known to be non-zero and positive [62, 82]. The flame structure does not change significantly with changes in W_{BC}; the radial flame position simply shifts to longer radius with a more positive boundary condition. The value for W_{BC} for the simulation is chosen to match the flame position observed with the temperature profile from the experiment. The expected value for W in the preheat zone (approximately 200 s^{-1} or 400 s^{-1}) is observed and is not strongly sensitive to W_{BC}.

To unify the presentation, the experimental measurements are mirrored to reconstruct the full flame image for comparison to the simulation results. The data is mapped

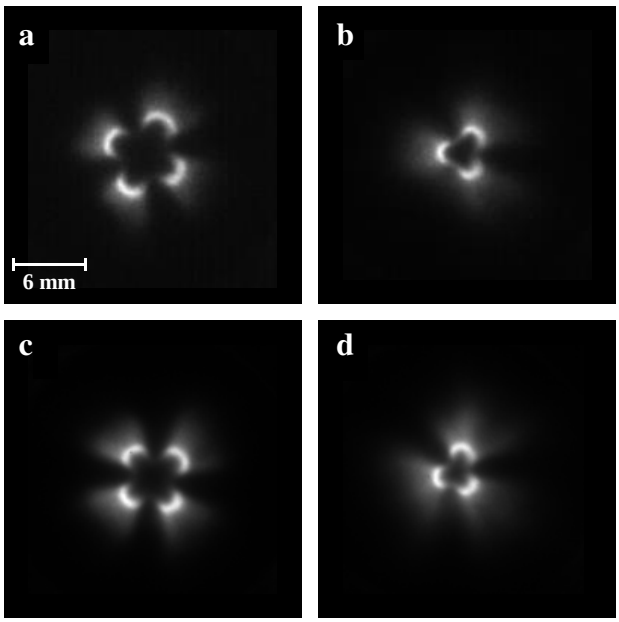

Figure 4.1 Chemiluminescence images showing cellular premixed cases listed in Table 4.1.

Table 4.1 Experimental conditions for premixed cellular tubular flames. Dimensions are: mole fractions for chemical species concentrations, $\frac{cm}{s}$ for radial velocity, and $\frac{1}{s}$ for stretch.

	O_2	N_2	CO_2	H_2	u_r	W_{BC}	Le	Φ	k
a	0.190	0.715		0.095	76.47	50	0.32	0.25	200.2
b	0.190	0.715		0.095	152.9	130	0.32	0.25	400.4
c	0.182		0.685	0.133	76.46	60	0.25	0.36	200.2
d	0.182		0.685	0.133	152.9	170	0.25	0.36	400.3

using radial basis functions [83–85], which permit straight forward interpolation with prescribed symmetry for reconstructing the flame structure over the entire spatial domain.

4.1 Low Stretch N_2 Dilution Case

Shown in Figure 4.2 are the experimental and numerical results for the 4 cell low stretch N_2 diluted flame (case **a** in Table 4.1). Qualitatively the comparison is excellent between numerical simulation and experiment, observed in the curvature of the flame cells and the distribution of the peak minor species number densities. Four flame cells are predicted, and the nature of the extinction zones can be confirmed to be thermal-diffusive in nature. The sharp "cusp" character of the extinction zone is observed in the O_2 and H_2O concentration maps and is not seen in the H_2 map; the hydrogen from the extinction zones is diffusing preferentially towards the cellular flame structures. This equivalence ratio enhancement is observed clearly, where the peak value is significantly higher than the boundary condition ($\Phi = 0.25$).

Quantitatively the differences are significant, observed in the temperature, H_2O, O_2, and Φ maps. The experimental equivalence ratio enhancement is consistent with the other discrepancies, where higher Φ results in: a hotter flame temperature, increased reactant consumption (O_2), and increased product generation (H_2O). This is confirmed by examining the temperature at the flame center ($r = 0$) and comparing it to the calculated adiabatic temperature of a H_2-air mixture with the same local equivalence ratio—experimental results show $\Phi = 0.43$ and $T = 1480\ K$ (adiabatic $T = 1489.6\ K$), and numerical results show $\Phi = 0.348$ and $T = 1306.4\ K$ (adiabatic $T = 1301.7\ K$).

While the equivalence ratio and temperature enhancement is consistent for each data set, a discrepancy of this magnitude is unexpected since the numerical simulation includes detailed kinetic and transport models. Additionally, a discrepancy in the temperature field is expected to affect minor species results, as the temperature and major species are required

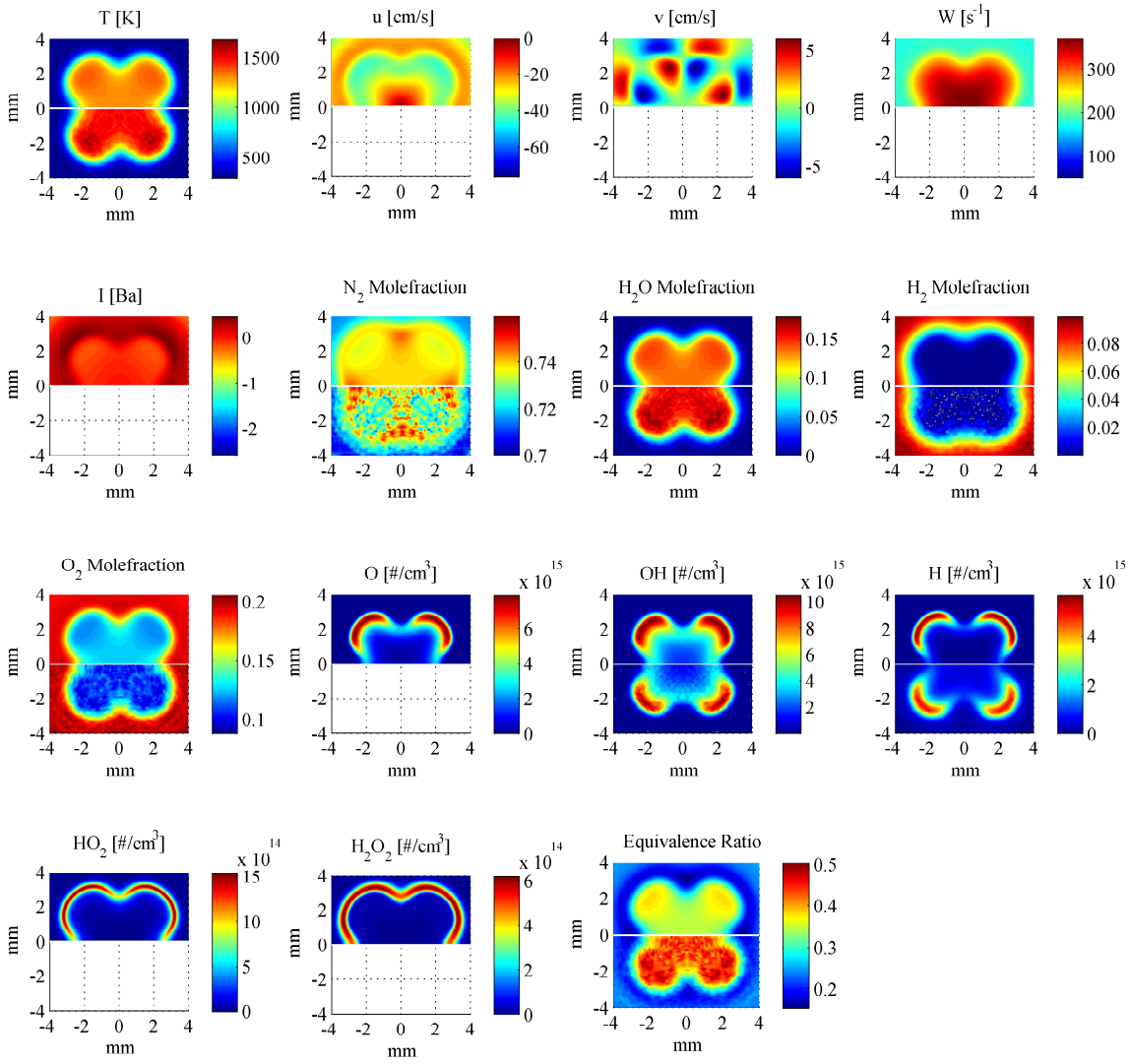

Figure 4.2 Comparison between numerical (top) and experimental (bottom) results for the low stretch N_2 diluted flame case **a** in Table 4.1

to report quantitative minor species concentrations due to collisional quenching corrections [31]. The other possibility is the inaccuracy of the boundary layer approximation; however, this approximation was found to work well for non-cellular flames of similar equivalence ratios and stretch rates [14, 30, 67]. For a clearer interpretation of these results, the other flame cases must be analyzed and compared.

4.2 High Stretch N_2 Dilution Case

Shown in Figure 4.3 are the experimental and numerical results for the 3 cell high stretch N_2 diluted flame (case **b** in Table 4.1). Similarly good agreement is found qualitatively with the comparison between simulation and experiments—the flame curvature, number of cells, and the thermal-diffusive mechanism (enhanced equivalence ratio in reaction cells) is observed. Interestingly, the same trends with qualitative discrepancies are found in this data-set as with the low stretch N_2 flame: temperature and equivalence ratio enhancements are under-predicted with simulation.

The more striking result is the similarity of the flame observables between the two N_2 dilution flame cases despite *doubling* the stretch rate. The experimental measurements for peak temperature, peak equivalence ratio, and peak minor species concentrations are all similar. This trend is not as pronounced in the simulation results, where the same observables increase slightly with doubling of the stretch rate. This leads to the hypothesis that the local cell curvature appears to be determining the enhancement of local equivalence ratio and therefore flame temperature. As seen in Figures 4.2 and 4.3, both experimental cases have flame cells of about the same local flame curvature. The simulation results also support this hypothesis, where the high stretch flame experiences slightly higher curvature.

To better understand the similarity between low and high stretch cases, the flame curvature was quantified experimentally and numerically. The flame boundary is defined with an isotherm that coincides with the peak chemiluminescence intensity (1350 K for

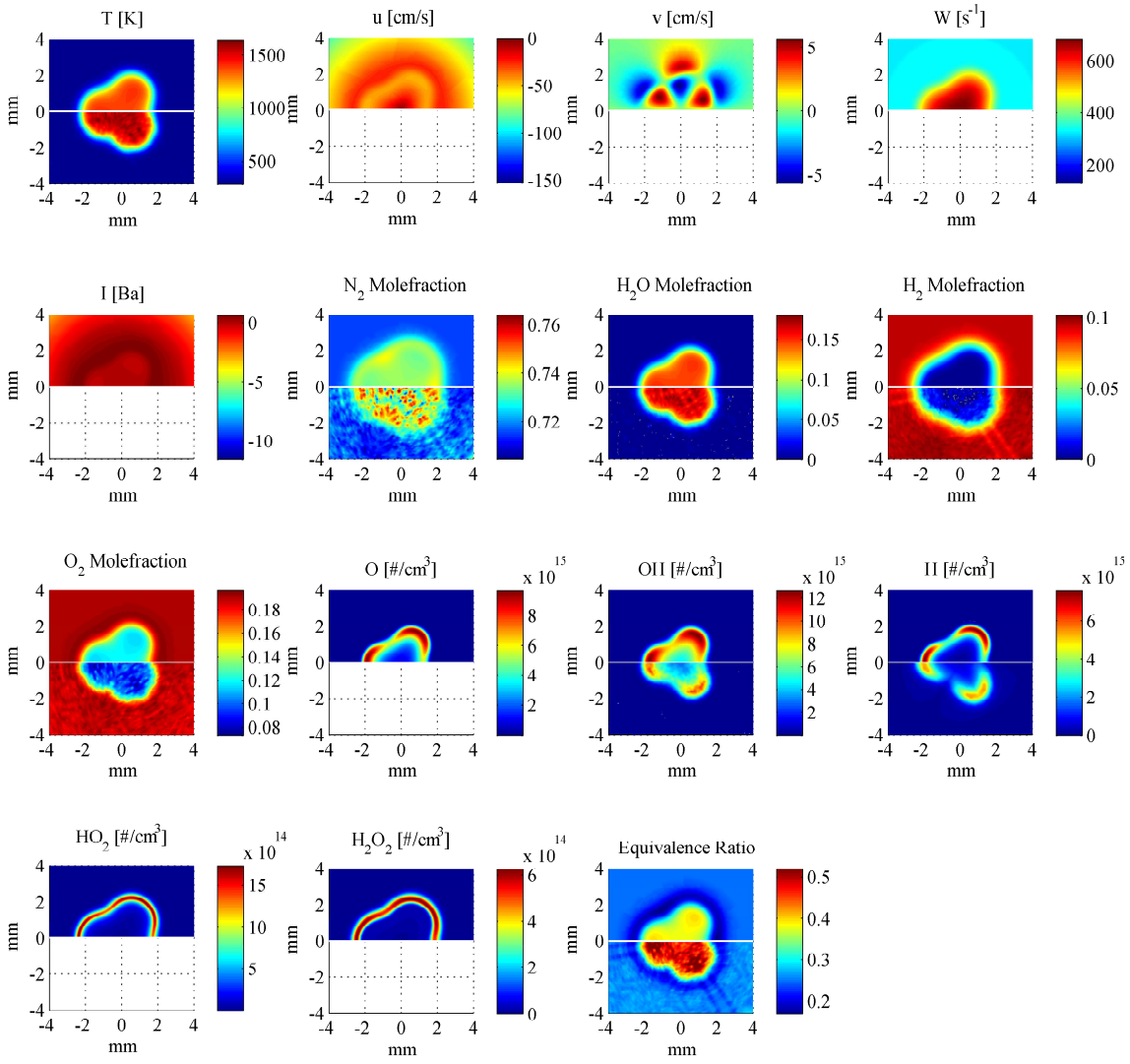

Figure 4.3 Comparison between numerical (top) and experimental (bottom) results for the high stretch N_2 diluted flame case **b** in Table 4.1

both experimental cases, 1223 K and 1245 K for low and high stretch simulation cases). For both the experiments and simulations, the curvature was found to be non-constant across the flame cell, where lower curvature is observed at cell center compared to the edges. This may be an artifact from the specific flame boundary, due to the sensitivity of flame parameters on specific flame surface definitions in experimental data [86]. Taking an average curvature value over the flame cell is estimated as being a more repeatable parameter, which was found to be approximately equal between the two stretch cases experimentally ($\sim$1 mm^{-1}) [87], and slightly higher for the high stretch ($\sim$1.22 mm^{-1}) vs. low stretch ($\sim$0.85 mm^{-1}) simulation result. It is noted that using a contour of the peak heat release would be a more accurate flame surface profile; however, this data is only present in the simulation results, and using an isotherm allows for the same flame surface definition between the experiment and simulation.

To the author's knowledge, an invariance (or approximate invariance) of local flame curvature with respect to stretch has not been reported. Curvature in non-cellular tubular flames is strongly dependent on stretch [14, 15], and previous research on cellular tubular flames [7, 15] does not quantify local cell curvature. The observed decoupling of stretch from curvature may be explained through the nature of the tubular flow-field—stretch is nonzero only along the axial direction, and the cellular structures only occur along the azimuthal direction. This orthogonality for tubular flames may be a cause for the observed independence of local curvature and stretch; in other premixed laminar burners, this decoupling is not possible. In spherical premixed flames, stretch acts along both dimensions of the flame surface and causes a thermal-diffusive cellular structure without regular patterns [5, 88]. In stagnation flow burners (opposed jet, stagnation jet, and tubular) stretch is unidirectional, although for all but the tubular burner, stretch forces azimuthal cellular states that experience variable cell widths (forming angular sections) [5]. For tubular flames, the cells form uniform "stripes" that experience uniform curvature.

4.3 Low Stretch CO_2 Dilution Case

Shown in Figure 4.4 are the experimental and numerical results for the 4 cell low stretch CO_2 diluted flame (case **c** in Table 4.1). Qualitatively the comparison is good, particularly with the curvature of the flame and the relative shapes of the temperature and major species plots. The flame cell curvature does not agree as well for the two minor species measured. The experimental measurements show flame cells with lower curvature at the center of the cell, and sharper curvature at the edges.

Quantitatively the comparison is good between the temperature profiles; however, the product generation, oxidizer consumption, and hydrogen enrichment (H_2O, O_2, Φ) in addition to one of the minor species (H-atoms) are all over-predicted. The difference in the measured and simulated OH peak values are well within the estimated experimental uncertainty ($\pm 2.0 \times 10^{15}$ cm^{-3}). From interpretation of the temperature field agreement, this flame condition experimentally results in a stronger flame with lower consumption of O_2 and lower equivalence ratio enhancement. This does not agree with intuition, as a lower Lewis number should prescribe a stronger equivalence ratio enhancement for a stronger burning flame.

Similarly as to what was done previously, the consistency is checked between the two data sets by comparing the temperature at the flame center ($r = 0$) to the calculated adiabatic temperature of an $H_2/O_2/CO_2$ mixture with the same local equivalence ratio and initial CO_2:O_2 ratio (3.76:1). Experimental results show $\Phi = 0.40$ and $T = 1230\ K$ (adiabatic $T = 1125.3\ K$), and numerical results show $\Phi = 0.530$ and $T = 1291.4\ K$ (adiabatic $T = 1336.4\ K$). The center-line temperature significantly disagrees with the adiabatic for both experiment (+100 K) and simulation (-45 K). This leads to the conclusion that the relative CO_2 content at the center-line changes—the preferential diffusion responsible for the equivalence ratio enhancement is also affecting the local dilution ratio.

It is noted that similar discrepancies were observed and not resolved with non-cellular CO_2 diluted tubular flames (shown in Figure 6 of reference [30]), where the CO_2

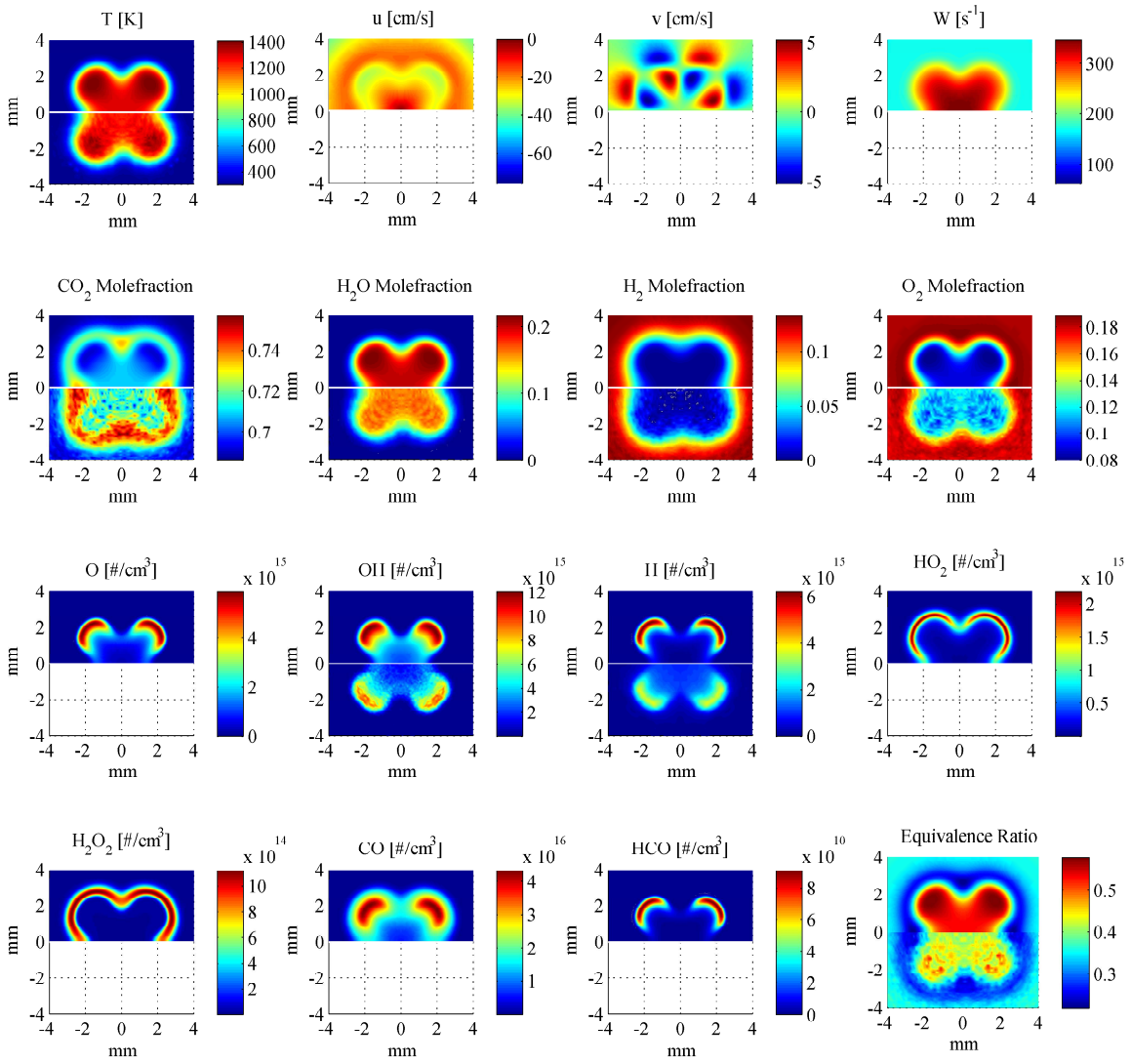

Figure 4.4 Comparison between numerical (top) and experimental (bottom) results for the low stretch CO_2 diluted flame case **c** in Table 4.1

concentrations at the origin were ill predicted.

4.4 High Stretch CO_2 Dilution Case

Shown in Figure 4.5 are the experimental and numerical results for the 3 cell high stretch CO_2 diluted flame (case **d** in Table 4.1). Qualitatively the comparison is good, with the cell curvature being predicted well for both the major species and temperature data as well as with the two minor species measurements. Qualitatively the observations are similar to the low stretch CO_2 case: the temperature is well predicted, the equivalence ratio enhancement, product generation, and oxidizer consumption are under predicted, and the H-atoms are over predicted. In contrast, the peak OH concentration is under-predicted, though the difference is comparable to the estimated experimental uncertainty ($\pm 2.0 \times 10^{15}$ cm^{-3}).

The doubling of the stretch rate does not significantly change the peak temperature or the flame cell curvature, agreeing with the trend observed from the two N_2 flame cases. This finding supports the hypothesis made previously based on the N_2 cases: curvature, not the stretch rate, is dominant in defining flame structure in this flow field. For a more in-depth analysis of the cellular structure, numerical experiments provide access to more complete data sets with conditions difficult to measure experimentally. With the observation of similar trends and good qualitative agreement between experimental and simulation results, the results from numerical experiments are expected to be valid.

4.5 Summary

Despite the quantitative discrepancy between the experimental and numerical results, comparison between each of the 4 cellular flame cases for either the numerical or experimental results yield similar observations. Aside from the number of cells, the flame structure is approximately invariant between cases with the same dilution gas—despite doubling the stretch rate the peak temperature, peak chemical species concentrations, and flame

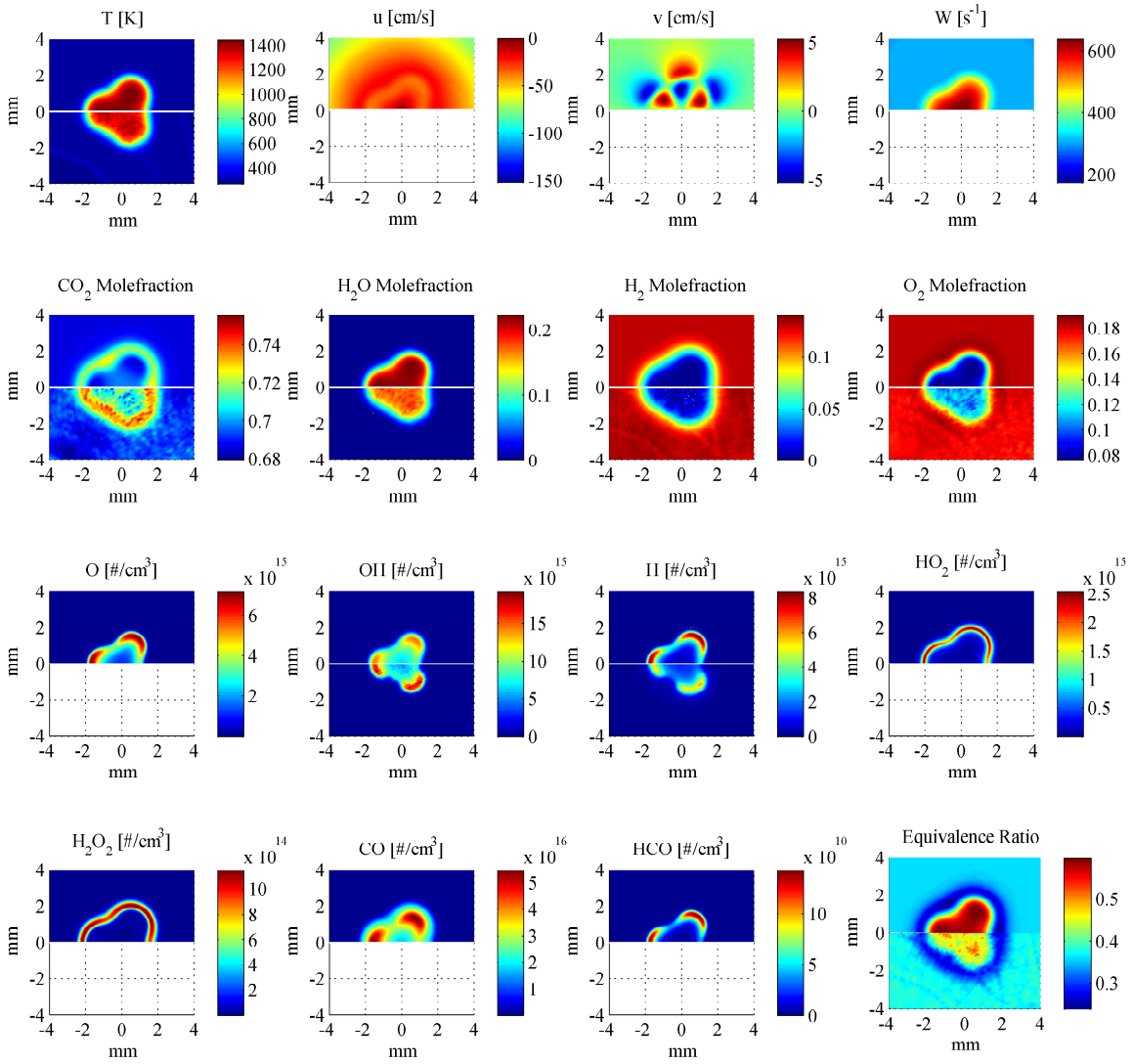

Figure 4.5 Comparison between numerical (top) and experimental (bottom) results for the high stretch CO_2 diluted flame case **d** in Table 4.1

cell curvatures are all very comparable. What appears to be local extinction (observed in H, OH, and O minor species plots) is actually zones of low temperature chemistry (observed in HO_2 and H_2O_2 plots). This observation implies that cellular flames could be useful experimental and numerical targets for future investigations of chemical kinetics, where the zones of different chemistry strongly test reduced mechanisms. Overall, these tubular cellular flame cases exhibit strong local curvature with apparent extinction zones that provide strong multidimensional spatial non-uniformity similar to practical turbulent flames in a laminar and time-steady environment.

CHAPTER V

NUMERICAL EXPERIMENTS

Analysis of flame structure is frequently easier with simulations as compared to experiments, as quantities that are commonly discussed can be difficult to directly measure (e.g. heat release rate), yet may be unambiguously derived from simulation results. What simulations can also provide is verification of whether or not specific experimental observables correlate with derived quantities. Cellular flames offer this luxury, and as an example the comparison of heat release rate and predicted chemiluminescence [19] is shown in Figure 5.1. The correspondence of these two quantities is exceptional, suggesting that for similar conditions the experimental imaging of chemiluminescence is sufficient for locating the flame reaction zone structure. Because of the low computational cost, further numerical experiments can be easily and quickly performed to investigate the quantitative correlation between other observable and derived flame quantities.

Here, the focus will be on the use of numerical experiments to: (1) examine the utility of cellular tubular flames for investigating practical phenomena, and (2) expand on the trends observed with the case study. This investigation will focus on the results from parametric studies performed with full detailed chemical kinetics and multicomponent transport, with the intention of drawing clear conclusions on the dominant phenomena responsible for the cellular structure.

5.1 Cellular Hysteresis

A topic found in fundamental flame research is investigating hysteresis and multiplicity using a variety of analytical techniques. These phenomena allow insight into tur-

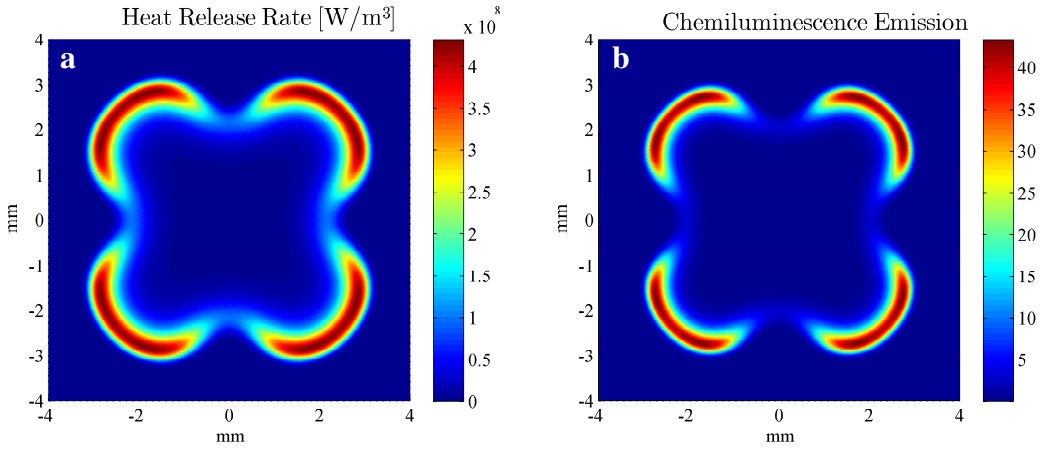

Figure 5.1 Numerical comparison between the heat release rate (a) and predicted chemiluminescence (b) for the low stretch N_2 diluted flame case **a** in Table 4.1

bulence by examining the mathematical stability of different flame surface structures. The tubular flame offers distinct advantages, as the spatial instability can be observed experimentally and is capable of being simulated with full detail. This flow field has been previously examined with local a linear stability analysis [89], and presumably could be examined with non-linear analyses (e.g. reference [90] for planar flames) which use fewer non-physical assumptions.

The use of the tubular cellular flame allows for clear and direct comparison between analytical and experimental results. Here, we examine the hysteresis found between cellular states when changing the equivalence ratio. This allows for a multiplicity of observed flame states (e.g. either a 3 or 4 cell case) for the same boundary conditions. The range over which this effect is experimentally observed is narrow, and only successive numbers of cells are observed to exist. This is replicated numerically with a parametric study on the boundary equivalence ratio.

The parametric study was performed with the low stretch N_2 dilution mixture (H_2-air, $k = 200\ s^{-1}$) in the full domain ($\theta \in [0, 2\pi]$), and scanned from a non-cellular flame case out to a 7-cell flame case. The equivalence ratio is scanned in steps of 0.005, first in the

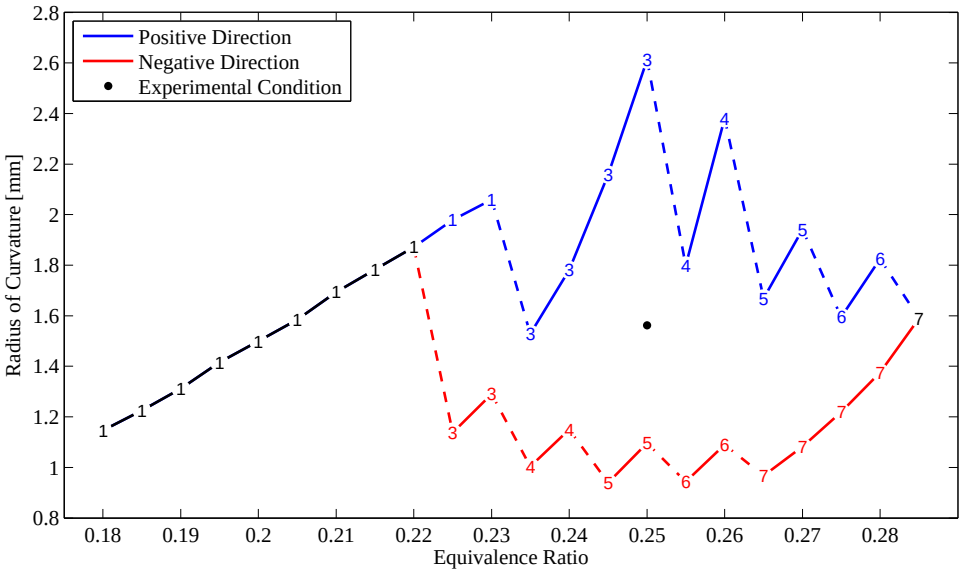

Figure 5.2 Hysteresis loop and multiplicity of the 200 s^{-1} N_2 case, when increasing the equivalence ratio from 0.18 to 0.285 (positive direction), followed by decreasing equivalence ratio (negative direction) back to the starting value. Black trends are where both the positive and negative directions obtained the same numerical solution. Here, "1" cell refers to the non-cellular flame.

positive direction ($0.180 \rightarrow 0.285$) and then in the negative direction ($0.285 \rightarrow 0.180$). The results are processed for radius of curvature at the center of the flame cell, using the contour of the peak heat release. This is shown in Figure 5.2 where: each solution is shown with a number for the number of cells, solid lines connect the solutions with the same number of cells, and dashed lines denote a solution process where the number of cells changed. The solid black lines denote that the same solution is obtained for either direction, and the black data point is the 4-cell solution found for the experimental boundary conditions.

The 4-cell flame condition is completely enveloped in the hysteresis loop, which is numerically predicted to be wider than found experimentally. This follows intuition, as the experiment suffers from more noise that is not present in the simulation (e.g. oscillations in flow rates or room vibrations). The specific utility for a hysteresis loop is the ability to

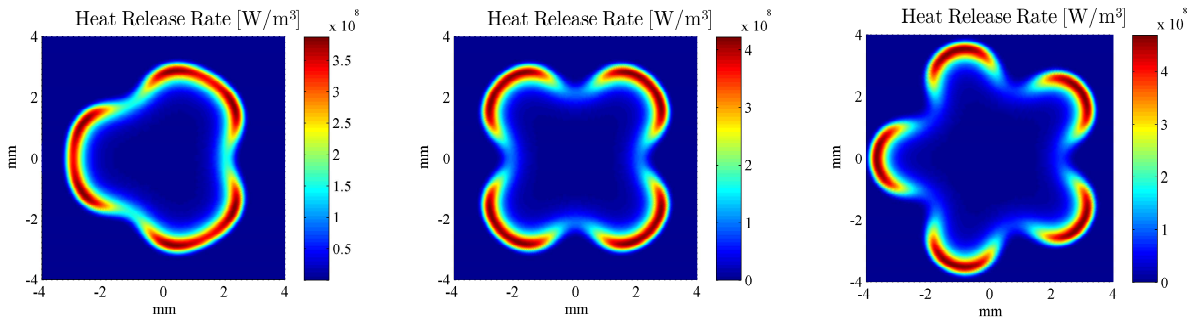

Figure 5.3 Heat release rates for three numerically predicted cellular states of the low stretch H_2-air cellular tubular flame case **a** in Table 4.1.

examine the flame cases that result from it—multiple flame states may be simulated for the same boundary conditions. This allows for clear comparisons of flame structure that omit any changes in the mixture.

The heat release plots of the three numerically predicted flame cases at $\Phi = 0.25$ (3, 4, and 5 cells) are shown in Figure 5.3. Both the cell curvature and the peak heat release increases with increasing numbers of cells. For a clearer comparison, the peak radial heat release is plotted in Figure 5.4 as a function of azimuthal angle for these flame cases—more cells correspond to a peak heat release that is higher in the cells, and lower in the extinction zones. This finding agrees with findings reported in literature, where sub-unity Lewis number flames are enhanced with more positive curvature. Cellular tubular flames simply provide a relatively simple flame geometry (2D structure) that can separate the effects of stretch and curvature, which is not available for cellular or non-cellular flames in other laboratory burners.

5.2 Dilution Gas Type

The relative significance of heat and mass diffusion is gauged broadly with the dimensionless Lewis number, which has been shown to be responsible for cellular flame struc-

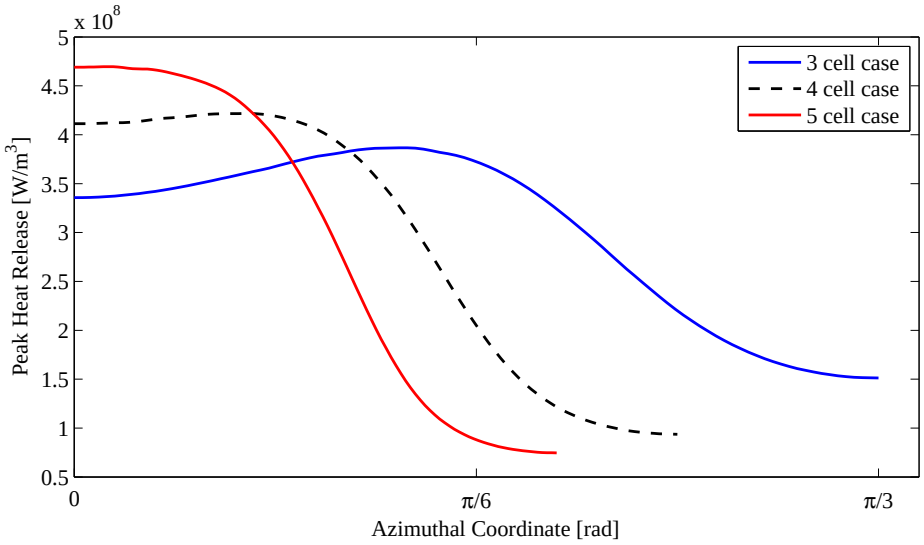

Figure 5.4 Peak radial heat release rates for the three numerically predicted cellular states of the low stretch H_2-air cellular tubular flame shown in Figure 5.3. The azimuthal coordinate is scanned from the cell center ($\theta = 0$) over to the extinction zone center ($\theta = \frac{\pi}{N}$) for each N-celled flame case.

ture: cells are only observed for Le < 1 [7]. What was found with this case study is that experimental flame curvature does not strongly depend to the dilution gas type (for the conditions considered). This result does not follow intuition, as a lower Lewis number should result in flame cells with higher curvature (lower radii of curvature) and higher thermal-diffusive enhancement. What has been investigated in the past is the transition points for different cell numbers as a function of dilution gas [7]. What numerical experiments can additionally provide is clear access to the curvature and transition behavior of the tubular cellular flames.

The parametric study was performed in equivalence ratio using the low stretch mixtures ($k = 200$ s^{-1}) of N_2 or CO_2 at the same dilution/oxidizer ratio (3.76:1) in the full domain ($\theta \in [0, 2\pi]$). For either mixture the simulation was scanned from a non-cellular flame case out to a 7 cell case, resulting in ranges of equivalence ratio of $[0.180, 0.285]$ for N_2 and $[0.24, 0.43]$ for CO_2 dilution. The equivalence ratio was scanned in different step

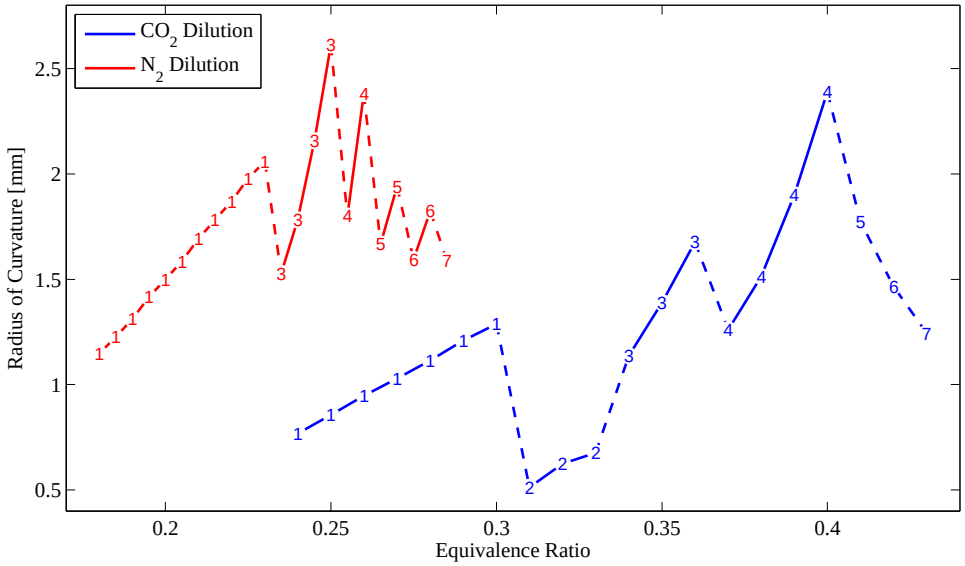

Figure 5.5 Effect of dilution gas type on cellular character, where the equivalence ratio is increased from non-cellular to 7 cells for a stretch rate of 200 s^{-1}. Here, "1" cell refers to the non-cellular flame.

sizes for either N_2 (0.005) or CO_2 (0.01) due to the different equivalence ratio ranges over which the cellular behavior covers. The results are processed for radius of curvature and are displayed in Figure 5.5 using the same technique discussed previously in Section 5.1.

What is immediately observed is that the lower Lewis number CO_2 mixture (Le $\sim$ 0.25) on average sustains cellular flames with lower radii of curvature compared to the N_2 mixture (Le $\sim$ 0.36), agreeing with intuition. As the equivalence ratio is increased the radius of curvature increases, eventually resulting in a transition to a higher number of cells with a lower curvature radius (neglecting the 2-cell cases). What is additionally observed is that for limited ranges of equivalence ratios, flames with the *same* number of cells can be obtained in both mixtures that have the *same* cell curvature. This agrees with the experimental observations, but extends the conclusion to show that the effect of Lewis number is to lower *on average* the curvature of the flames for all numbers of cells.

The main discrepancy observed is the existence of the 2-celled case for only the CO_2 cases. This flame geometry is observed experimentally for both dilution gasses; however, they can be difficult to conclusively discern from a non-cellular geometry [7], and they tend to quickly transition to a 3 cell state. The existence of these cases in only one of the parametric studies to assumed to be due to the incomplete nature of the simulation algorithm for tracking symmetry transitions. The solution process used here solved successive cases using the previous solution as the initial condition. For a more thorough examination of the existence of different symmetry states and the exact transition points between them, the solution algorithm would require modification for stabilization to track these phenomena specifically [91].

5.3 Effect of Stretch Rate

The investigation of stretch rate on the structure of flames is a common topic, which is essential for building computationally efficient approximations to chemical kinetics in practical flames (e.g. see references [2,92]). The cellular tubular flame allows for investigations with less restriction on the flame curvature. The non-cellular geometry prescribes the curvature as a function of stretch rate (due to the stagnation point velocity field); cellular geometries allow the individual cells to adapt to the flow field similar to realistic flames in practical burners.

The parametric study was performed in stretch rate using the two mixtures found from the study in section 5.2 that resulted in 7 cell cases at $k = 200$ s^{-1}: $\Phi = 0.285$ for N_2 and $\Phi = 0.43$ for CO_2 dilution. The simulation is performed in the full domain ($\theta \in [0, 2\pi]$), and the stretch rate is increased in steps of 25 from k =200 to 750 s^{-1}. The results are processed for radius of curvature and are displayed in Figure 5.6 using the same technique discussed previously in Section 5.1.

The strongest difference between the two mixtures is the increments for cell number

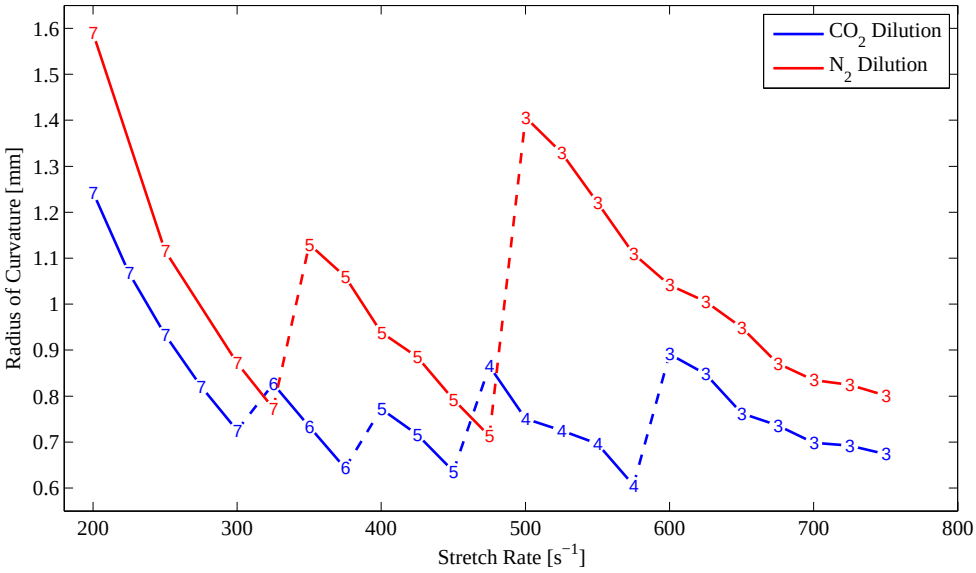

Figure 5.6 Effect of increasing the stretch rate from 200 to 750 s^{-1} on the cellular character for two different dilution gasses: Φ =0.285 for N_2 and Φ =0.43 for CO_2.

transitions: CO_2 flames decrease in cell number by 1 and N_2 flames by 2. This trend has not been reported in experiments; however, it is likely that parametric studies similar to this have not been performed experimentally. In the past it has been difficult to change the stretch rate without varying the equivalence ratio in the process; with the experimental setup developed during the course of this work, simultaneous control of all gas mass-flow controllers is possible for this type of experiment.

The second strong observation from the results in Figure 5.6 is that the lower Lewis number CO_2 mixture results in flame cells with a lower radius of curvature on average as compared to the N_2 dilution. However, the experimental trend is also observed—for specific conditions flames with *different* numbers of cells and/or a *different* dilution gas can exist with the *same* flame curvature. This aspect of numerical and experimental investigations cannot be overstated: conflicting observations can be made with incomplete data sets. If we were to rely only on the results from the brief parametric study, incorrect conclusions

could be drawn. A more complete case study with many more experiments can provide evidence for stronger conclusions; however, numerical experiments are less expensive and can provide results that guide the experimental design for more focused future experimental studies.

5.4 Summary

As found from the three parametric studies, numerical experimentation is a valuable tool to interpret or guide experimental campaigns. The low expense of tubular cellular simulations (relative to detailed experimental campaigns) allows for exploration to discover flame conditions that show high sensitivity to desired observable phenomena. Here, the numerical experiments were performed to characterize the effect of the controlled variables (stretch rate, equivalence ratio, and dilution gas type) on the flame appearance (curvature and number of cells). All of the findings are consistent with the hypothesis that the flame curvature, not stretch rate, is dominant in determining flame structure for the mixtures considered.

The importance of experimental and numerical case studies cannot be neglected—results from the numerical simulation do not match all of the experimental measurements and the discrepancies have not all been reconciled. The accuracy of the numerical simulations and the numerical experiments is good within the bounds of the simulation: accuracy of the kinetic rate parameters, diffusive transport parameters, and/or the boundary layer assumption. It remains unclear from non-cellular work which of these effects is the dominant, as the discrepancy with the experiment is significantly higher than the estimated measurement uncertainty.

CHAPTER VI

TRANSPORT APPROXIMATIONS

As found from the case study and numerical experiments, the structure of flame cells is strongly related to the thermal-diffusive properties of the mixture. Thus, cellular tubular flames are attractive for investigating the accuracy of diffusive transport approximations, as the structure should be highly sensitive to the accuracy of transport models. The two common approximations found in literature are examined here: (1) neglecting thermal diffusion and (2) using a mixture-averaged approximation for dominant transport fluxes (heat, mass, and momentum). These assumptions have previously been examined with detailed 1D [56,93] and 2D [57,94,95] simulations, which all arrive at similar conclusions: thermal diffusion can be important in predicting quantitative flame structure, thermal diffusion is dominated by the Soret effect, and the mixture-averaged approximation is valid for dilute mixtures.

For clarity of discussion: (1) we restrict our initial analysis to the 4-cell N_2 flame case **a** in Table 4.1, and (2) we define acronyms to label simulation cases based on the specific diffusive transport model. The overall form of diffusive transport is either multicomponent (MC) or the mixture-averaged approximation (MA), and simulation cases may include or neglect thermal diffusion (TD). Then, the most accurate simulation result is multicomponent with full thermal diffusion (MC-TD), and the most common modeling simplification is mixture-averaged with no thermal diffusion (MA).

The most common approximation, neglecting thermal diffusion, is significant and is shown in Figure 6.1 by comparing the MC-TD case against the MC case. The flame cells exhibit qualitatively different flame appearance and substantially lower flame strength if thermal diffusion is not included. Also found is that thermal diffusion is dominated by

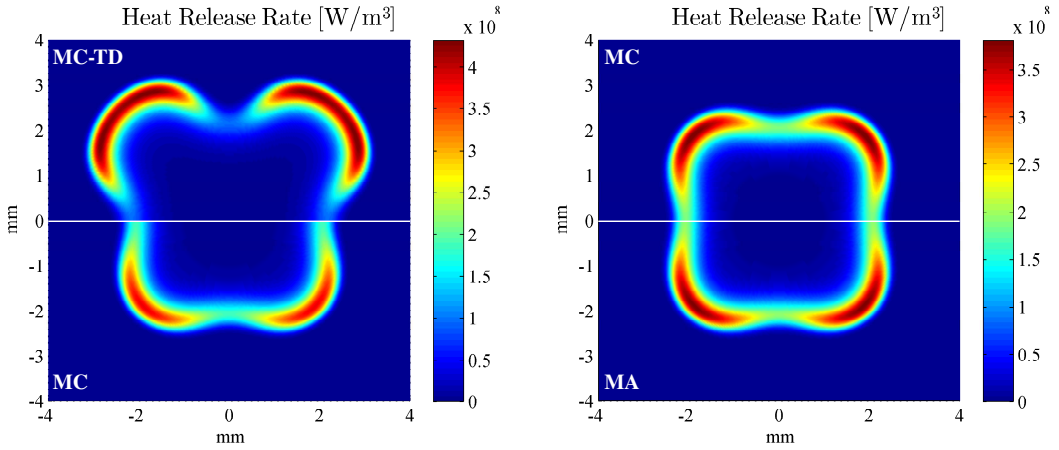

Figure 6.1 Comparison of heat release rates for different diffusive transport approximations on the low stretch H_2-air cellular tubular flame case **a** in Table 4.1. The comparisons are for multicomponent (MC) or mixture-averaged (MA) transport optionally including thermal diffusion (TD).

the Soret effect; neglecting only the Dufour effect causes negligible change to the flame appearance. This finding agrees with conclusions reported in literature [56, 57].

The next common approximation is to use mixture-averaged forms for the primary transport coefficients ($\mu, \lambda, \mathcal{D}_{ij}$). Shown in Figure 6.1 are the simulation results neglecting thermal diffusion comparing the MC case against the MA case. The difference between the two formulations is negligible, again agreeing with conclusions reported in literature [56,57] and supporting the common practice of using a mixture-averaged approximation. However, without thermal diffusion, the flame structure is inaccurate. Including thermal diffusion requires the calculation of the multicomponent form of heat conductivity (λ), and to the best of the authors' knowledge, an approximate formulation of thermal diffusion is not widely accepted. The only approximations found are sparse in literature and are "semi-empirical" formulations (e.g. see discussion in reference [56]). The most accessible approximation is the thermal diffusion ratio $\widetilde{\chi}_i$ provided by `CHEMKIN`, for which even the documentation states as "considerably less accurate than the thermal diffusion coefficients that are computed from

the multicomponent formulation" [47]. What would be most beneficial for large-scale computations is an accurate but computationally inexpensive approximation for thermal diffusion.

6.1 Approximating Thermal Diffusion

In order to access the practical functional dependence of thermal diffusion, the coefficients are calculated for several flame cases using Equation 3.9b and are shown in Figure 6.2 for each chemical species as a function of temperature. The flame cases shown are full transport (MC-TD) and consist of: both N_2 cellular tubular flame conditions and two cases of a lean H_2-air 1D premixed flame [96]. The uniformity of the coefficients is excellent over the spatial domains and across the two flame types. Furthermore, the dominant coefficients correspond to the lightest chemical species (H and H_2), and are an order of magnitude more significant than all other species. This importance of light species is in agreement with findings reported in literature [93], and supports the notion that a modeling approach concerning only H and H_2 would be sufficiently accurate.

Shown in Figure 6.3 are the different formulations of the H and H_2 thermal diffusion coefficients for the 4 cell flame case. Shown in black are the multicomponent coefficients calculated with Equation 3.9b, and in red are the semi-empirical coefficients calculated with Equation 3.11b. The accuracy of the semi-empirical model is poor, motivating the use of a simple polynomial fit for a better approximation,

$$\mathcal{D}_i^T \approx \sum_{n=1}^{M} c_{i,n} T^n, \qquad m_i < 5 \tag{6.1}$$

where $c_{i,n}$ are M static coefficients for each species i, and only the light species (H, H_2) are considered. The form of the polynomial is chosen to simplify the expression of thermal diffusion. For a single parameter fit, the thermal diffusion term in Equation 3.4b simplifies

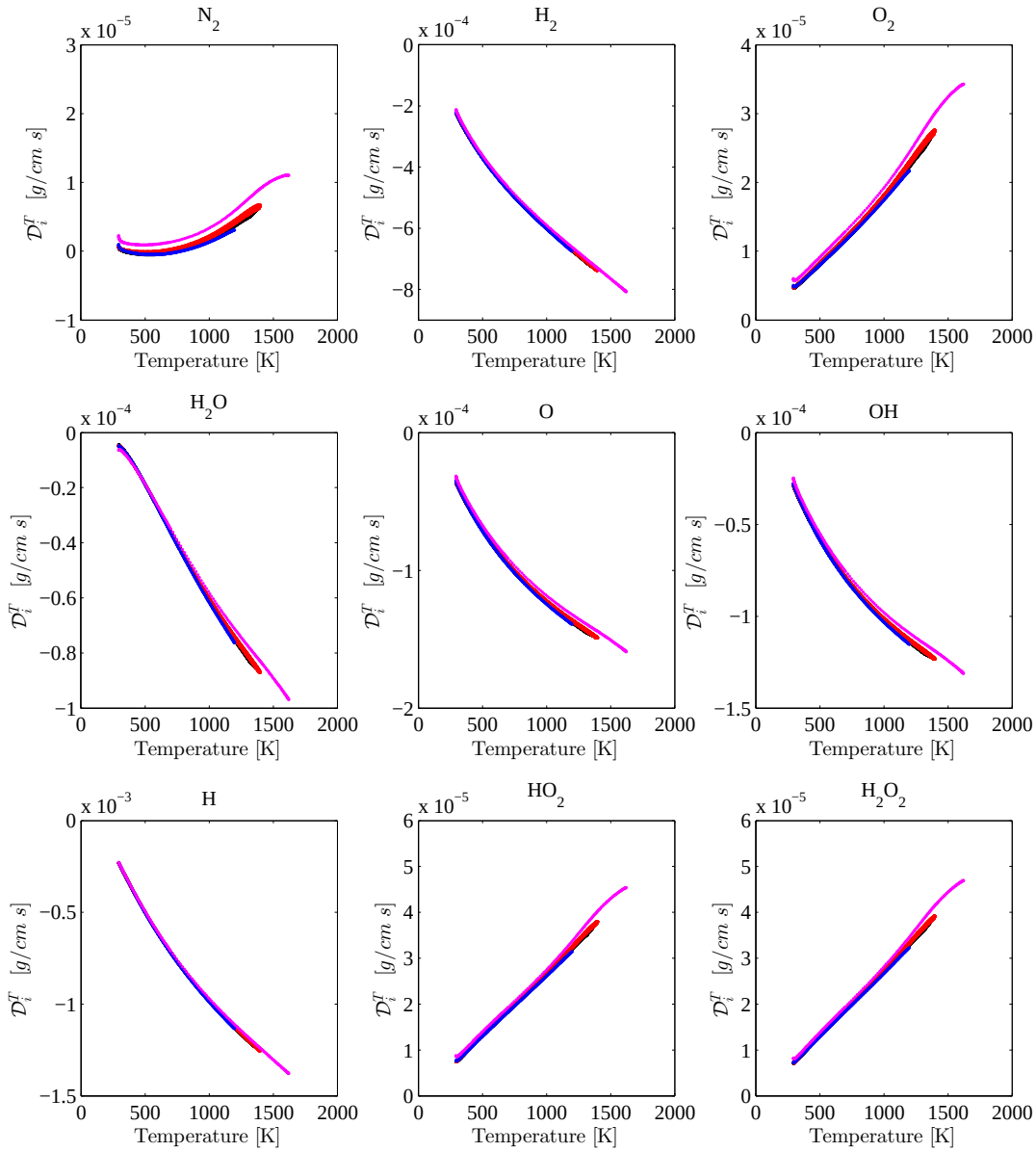

Figure 6.2 Shown are the thermal diffusion coefficients for different MC-TD flame simulations. Both N_2 dilution cellular tubular flames are shown: low stretch is shown in black and high stretch is shown in red. One-dimensional premixed flame simulations [96] are shown for comparison: $\Phi = 0.30$ is shown in blue and $\Phi = 0.50$ is shown in magenta. Note that the data sets overlap and obscure each other.

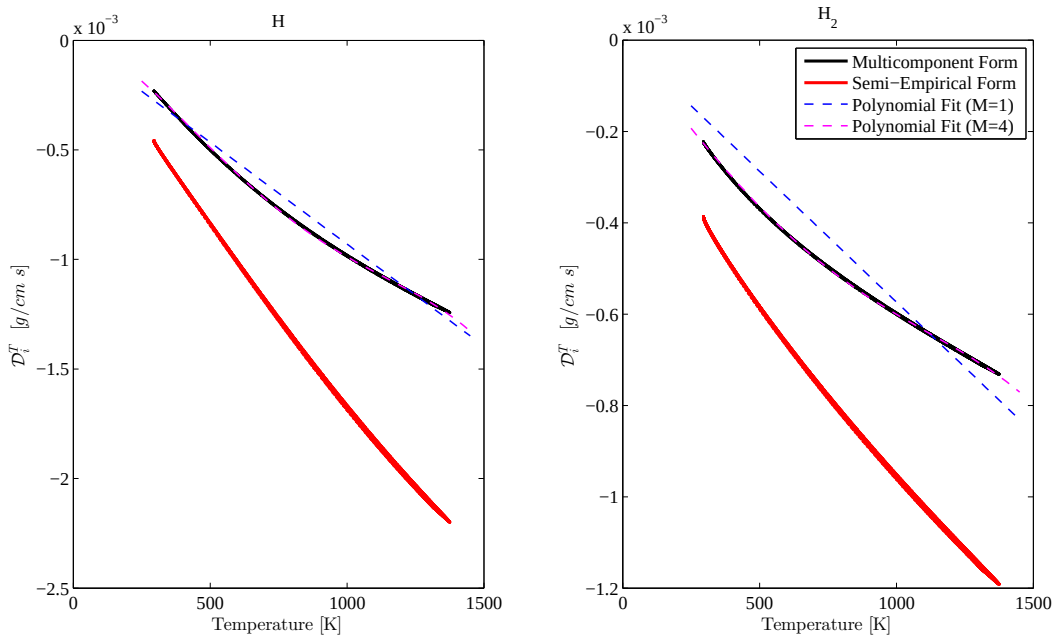

Figure 6.3 Shown are the thermal diffusion coefficients for H and H_2 for different levels of approximation calculated from the simulation results of the low stretch H_2-air cellular tubular flame case **a** in Table 4.1.

to

$$Y_i \mathcal{D}_i^T \nabla \ln T \approx Y_i c_{i,1} \nabla T \tag{6.2}$$

and for a higher order fit the term is expressed as

$$Y_i \mathcal{D}_i^T \nabla \ln T \approx Y_i \left(c_{i,1} + c_{i,2} T + \ldots + c_{i,M} T^{M-1} \right) \nabla T \tag{6.3}$$

This polynomial form is shown in Figure 6.3 for two orders of fit: the single parameter fit ($M = 1$) is the dashed blue line and a high order fit ($M = 4$) is the dashed magenta line. The high order fit is indistinguishable from the multicomponent coefficients, while even the linear fit is substantially more accurate than the semi-empirical model.

To use this approximation in realistic simulation codes, the polynomial fitting coefficients $c_{i,n}$ would need to be determined. In lou of theory to predict the values, prior calculations of the flame structure would be required to provide data for the fit. However, the true multicomponent thermal diffusion coefficients $\mathcal{D}_i^T$ can be calculated from *any* data set using Equation 3.9b, *including data sets that use approximate transport models*. Excellent correspondence is found between multicomponent thermal diffusion coefficients calculated from the cellular flame simulation cases with full (MC-TD) and approximate (MA, MC) transport. All the thermal diffusion coefficients collapse to the same trend, corresponding to the black traces in Figure 6.3. This observation allows for the use of preexisting or preliminary results to support a practical simulation that includes an accurate and inexpensive approximation of thermal diffusion.

To compare the observable accuracy of the approximate thermal diffusion models, simulations were performed with mixture-averaged diffusive transport combined either with the semi-empirical `CHEMKIN` model, the linear model from Equation 6.1, or the fourth order model from Equation 6.1. The coefficients $c_{i,n}$ are fit using least squares to the MC-TD case data in Figure 6.3 and take the two forms: for the linear model,

$$\mathcal{D}_i^T \approx \begin{cases} -5.731E-07 \cdot T & \text{for } H_2 \\ -9.303E-07 \cdot T & \text{for H} \end{cases} \tag{6.4}$$

and for the fourth order model,

$$\mathcal{D}_i^T \approx \begin{cases} -7.751E^{-}07 \cdot T - 8.080E^{-}11 \cdot T^2 + 4.423E^{-}13 \cdot T^3 - 1.867E^{-}16 \cdot T^4 & \text{for } H_2 \\ -2.475E^{-}07 \cdot T - 2.606E^{-}09 \cdot T^2 + 2.724E^{-}12 \cdot T^3 - 8.579E^{-}16 \cdot T^4 & \text{for H} \end{cases} \tag{6.5}$$

where $\mathcal{D}_i^T$ is in units of $[g/cm\ s]$ and T is in $[K]$. The results for the 4 cell case are shown in Figure 6.4 compared against the full multicomponent solution with thermal diffusion. The

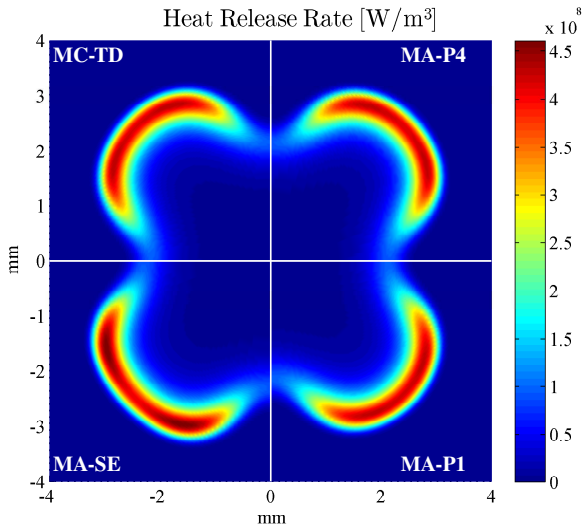

Figure 6.4 Comparison of heat release rates for different diffusive transport approximations on the low stretch H_2-air cellular tubular flame case **a** in Table 4.1. The comparisons are for full multicomponent case (MC-TD) against different mixture-averaged cases: the polynomial model of Equation 6.4 (MA-P1), the fourth-order polynomial model of Equation 6.5 (MA-P4), and the `CHEMKIN` semi-empirical model (MA-SE).

correspondence is excellent between the full multicomponent result (MC-TD), the fourth order approximation (MA-P4), and the linear approximation (MA-P1). The agreement is close between the full multicomponent result (MC-TD) and the semi-empirical `CHEMKIN` thermal diffusion (MA-SE), but the latter predicts higher flame strength and slightly different flame cell geometry. This discrepancy may not be deemed significant for some researchers; however, in some mixtures the semi-empirical model reportedly predicts even the wrong sign for the thermal diffusion terms [56]. This could not happen with the polynomial model implemented here, as the coefficients are determined from direct calculations.

6.2 CO_2 Dilution Results

The same trends are found for the CO_2 diluted flame cases—the polynomial fits from Equation 6.1 are accurate, and the fourth order fit is indistinguishable from the full

multicomponent solution. The coefficients of the polynomial fits differ from the N_2 case and take the forms: for the linear model,

$$\mathcal{D}_i^T \approx \begin{cases} -7.222E-07 \cdot T & \text{for } H_2 \\ -1.094E-06 \cdot T & \text{for H} \end{cases} \tag{6.6}$$

and for the fourth order model,

$$\mathcal{D}_i^T \approx \begin{cases} -5.466E^{-}07 \cdot T - 1.171E^{-}09 \cdot T^2 + 1.387E^{-}12 \cdot T^3 - 4.460E^{-}16 \cdot T^4 & \text{for } H_2 \\ 2.468E^{-}07 \cdot T - 3.798E^{-}09 \cdot T^2 + 3.347E^{-}12 \cdot T^3 - 9.477E^{-}16 \cdot T^4 & \text{for H} \end{cases} \tag{6.7}$$

These are shown graphically, along with the multicomponent and semi-empirical forms, in Figure 6.5. Again, the semi-empirical form over estimates the magnitude of thermal diffusion by almost a factor of 2.

The most significant difference between the thermal diffusion coefficients for flames in the CO_2 mixture verses the N_2 mixture is the slopes. The CO_2 mixture has steeper coefficients that result in stronger thermal diffusion as compared to the N_2 mixture. The same conclusion found for cellular flames in the N_2 mixture is supported by analysis of the CO_2 mixture: the coefficients are independent of the local mixture variations throughout the flame. Once the thermal diffusion coefficients are calculated from preliminary simulations that use a representative gas mixture, the polynomial fit given in Equation 6.1 may be used to include accurate and computationally inexpensive thermal diffusion effects.

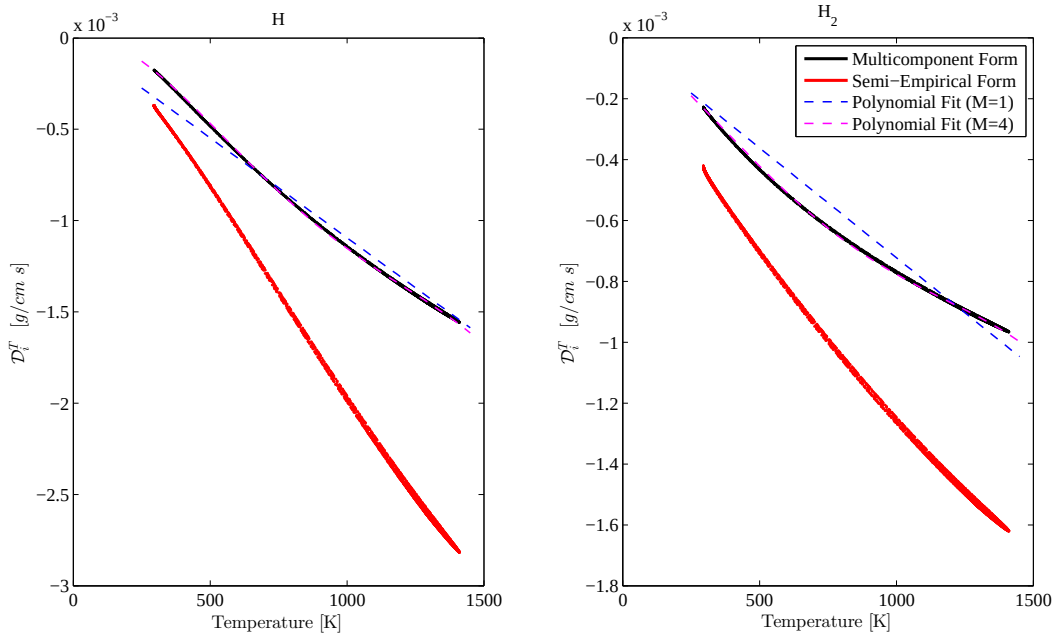

Figure 6.5 Shown are the thermal diffusion coefficients for H and H_2 for different levels of approximation calculated from the simulation results of the low stretch CO_2 dilution flame case **c** in Table 4.1

CHAPTER VII

CONCLUSIONS

The premixed cellular structures found in tubular flames were characterized using joint experimental and numerical approaches. Quantitative measurements of major species, temperature, and H-atom and OH concentrations are reported for the first time in cellular tubular flames. The major species and temperature measurement campaign provided evidence that supports the importance of diffusive phenomena (specifically heat and mass) on cellular flame structure. Preferential diffusion of molecular hydrogen from the extinction zones into the reaction cells is observed, with significantly enhanced temperatures and equivalence ratios in the cells. The minor species measurement campaigns provide evidence that supports the utility of H-atom measurements (now experimentally accessible with fs two-photon LIF [36]) as an indicator for flame zones.

The numerical model for 2D cellular tubular flames was developed and implemented with detailed chemical kinetics and multicomponent diffusive transport. The simulation code was used to provide predicted cellular flame structure to compare against experimental case data, and was then used to perform parametric studies to examine the effects of experimental variables on the flame appearance. The case comparison between experimental and numerically predicted temperature and chemical species fields show good agreement with flame appearance, but show significant discrepancies with quantitative flame structures. The trends observed experimentally are confirmed with numerical experiments: under specific conditions the cellular curvature is insensitive to stretch rate and dilution, but on average increasing stretch and decreasing the Lewis number leads to higher flame curvature.

Lastly, the numerical simulation code was used to show the importance of validating diffusive transport approximations commonly used in combustion simulations. Thermal

diffusion was found to be critical for accurate predictions of the lean diluted H_2 flames studied here, and is expected to be important for other flame geometries with sub-unity Lewis numbers. This conclusion is found elsewhere in literature [56, 57], but thermal diffusion currently does not appear to be included in many flame simulations due to the perceived numerical cost. As shown here, the thermal diffusion coefficients may be approximated well with a simple linear model, the coefficients of which can be predicted from previous simulation results that use mixture-averaged transport and exclude thermal diffusion. This has the important implication that *any available data set* (from 1D laminar flames up through 3D time dependent turbulent flames) can be used to check the validity of the simple linear thermal diffusion approximation discussed here.

The combination of experimental and numerical investigations for characterization of flame cases is powerful. As shown here with cellular tubular flames, much can still be learned about combustion from simplified flame cases and applied towards the understanding of combustion under practical conditions. Tubular cellular flames offer complex structure with relatively simple experimental and numerical requirements. The quantitative disagreement should be further investigated with future work utilizing different mixtures and different tubular flame types (e.g. non-premixed and partially premixed); however, the strong correspondence of overall flame shape and the ability to perform numerical experiments justify the development of this cellular tubular flame simulation. The symmetric 2D flame structure combined with the presence of extinction zones, reaction cells, and varying flame curvature, make cellular tubular flames ideal for validating modeling approximations used in practical simulations.

7.1 Suggestions for Future Work

This work provides the framework for future investigations of cellular tubular flames. The implementation of the 2D scanning Raman scattering and LIF experimental setups, combined with the development of the 2D numerical code, allows for further experimental

and numerical campaigns to be performed in tandem to quickly diagnose discrepancies and find specific flame cases that exemplify phenomena of interest.

Further experimental work is needed to investigate the quantitative agreement of the numerical simulation with the experimental results. Suggested future work includes:

- Examining more premixed cases using: different fuels, wider ranges of equivalence ratios, and additional dilution gas types
- Examining different flame types (e.g. non-premixed and partially-premixed) to further investigate the accuracy of the 2D simulation formulation
- Examining the temperature discrepancy in the N_2 diluted flame cases in more detail, e.g. with a different experimental measurement method

Additional numerical simulation campaigns would be highly beneficial, and further development of the numerical code could widen the scope of future simulation campaigns. Suggested future work includes:

- Modification of the code to permit branch tracing [91], in order to follow the detailed evolution of the cellular flame when changing the number of cells (i.e. turning points and unstable solution branches)
- Revision of the code to eliminate the need for boundary conditions at the coordinate origin, in order to allow for accurate solutions of non-symmetric cellular flames
- Modification of the code to resolve time dependent solutions, involving revision of the pseudo-transient continuation formulation and the evolution of the adaptive mesh to permit accurate time stepping

APPENDIX A

RAMAN SCATTERING UNCERTAINTY ANALYSIS

The measurement uncertainty of the Raman measurements (chemical species number densities and temperature) is estimated using the Kline-McClintock method [34]. This provides an estimate of the uncertainty (σ) of the derived variable (f) as a function of the uncertainties of the observed variables (x_i),

$$\sigma_f^2 = \sum_i \left(\frac{\partial x_i}{\partial f} \sigma_{x_i} \right)^2$$

A.1 Chemical Species Number Density

The simplified governing equations for Raman scattering are,

$$s_i = E K_{i,i} N_i \tag{A.1a}$$

$$N_i = x_i N_T = x_i \frac{p_0}{k_b T} \tag{A.1b}$$

$$s_i = s_{T,i} - s_{B,i} \tag{A.1c}$$

where E is the average integrated pulse energy, K is the calibration matrix, N is the number density, x is the mole fraction, p_0 is the thermodynamic pressure, k_b is the Boltzmann constant, T is temperature, s is the integrated Raman signals, the subscript i is for species specific values, the subscript T is for the total value, and the subscript B is the background value.

When performing the partial differentiation, the following derivative rule is noted,

$$\text{for } y = \prod x_i^{n_i}, \qquad \frac{\partial y}{\partial x_i} = \frac{1}{n_i}\frac{y}{x_i}$$

which allows for compact expressions of uncertainty. The estimated uncertainty for number density can then be expressed in the form,

$$\left(\frac{\sigma_N}{N_T}\right)_i^2 = x_i^2 \left[\left(\frac{\sigma_s}{s}\right)_i^2 + \left(\frac{\sigma_E}{\langle E\rangle}\right)^2 + \left(\frac{\sigma_K}{K}\right)_i^2\right] \tag{A.2}$$

The uncertainty from the coefficient matrix (σ_K) is derived the calibration procedure,

$$\left(\frac{\sigma_K}{K}\right)_i^2 = \left(\frac{\sigma_s}{s}\right)_i^2 + \left(\frac{\sigma_E}{\langle E\rangle}\right)^2 + \left(\frac{\sigma_N}{N}\right)_i^2$$

which is combined with Equation A.2 to arrive at,

$$\left(\frac{\sigma_N}{N_T}\right)_i^2 = x_i^2 \left[\left(\frac{\sigma_s}{s}\right)_i^2 + \left(\frac{\sigma_E}{\langle E\rangle}\right)^2\right] + x_i^2 \left[\left(\frac{\sigma_s}{s}\right)_i^2 + \left(\frac{\sigma_E}{\langle E\rangle}\right)^2 + \left(\frac{\sigma_N}{N}\right)_i^2\right]_{cal} \tag{A.3}$$

From this form of the uncertainty, specific aspects of the experiments and calibrations are included in the expression. First, the signal uncertainty (σ_s) is lower in the calibration due to greater binning: the experiment bins 2 superpixels per spatial location and calibration bins all 140 pixels. The binning scales the uncertainty with Poisson statistics,

$$(\sigma_s)_{cal} = \sqrt{\frac{2}{140}}\,(\sigma_s)$$

Second, the uncertainty for the mass flow controllers is taken as half of the accuracy (1% full scale) and for the energy detector is taken as half of the instrument resolution (1%).

$$\left(\frac{\sigma_N}{N}\right)_{cal} = \tfrac{1}{2}\left(0.01\left\langle\tfrac{\dot{m}_{max}}{\dot{m}}\right\rangle\right) \tag{A.4a}$$

$$\left(\frac{\sigma_E}{E}\right) = \tfrac{1}{2}\left(0.01\right) \tag{A.4b}$$

The form uncertainty from Equation A.3 may then be expressed as

$$\left(\frac{\sigma_N}{N_T}\right)_i^2 = \frac{71}{70}\left(\frac{k_b T \sigma_{s,i}}{p\left\langle E\right\rangle K_i}\right)^2 + x_i^2\left[2\left(0.005\right)^2 + \left(0.005\left\langle\frac{\dot{m}_{max}}{\dot{m}}\right\rangle\right)^2\right] \tag{A.5}$$

With the reasonable approximation of the nominal flow through the flow controllers during calibration to be approximately 71%, then

$$\left(\frac{\sigma_N}{N_T}\right)_i^2 = \frac{71}{70}\left(\frac{k_b}{p\left\langle E\right\rangle K_i}\right)^2 T^2\sigma_{s,i}^2 + \left(10^{-4}\right)x_i^2$$

The uncertainty from the signal is from noise associated with the CCD chip. The known (and checked) form of the noise is that of Poisson statistics, with the factor of the number of spatial pixels that are summed to

$$\sigma_s = \sqrt{N_\lambda s_T}$$

then the final form of the Raman scattering number density uncertainty is:

$$\left(\frac{\sigma_N}{N_T}\right)^2 = \frac{71}{70}\left(\frac{k_b}{p\left\langle E\right\rangle K_i}\right)xT + \frac{71}{70}\left(\frac{k_b}{p\left\langle E\right\rangle K_i}\right)^2 T^2 s_b + \left(10^{-4}\right)x_i^2 \tag{A.6}$$

A.2 Temperature

Writing Equation A.1b in terms of temperature,

$$T = \frac{p}{k_b N_T} = \frac{p}{k_b}\left(\sum N_i\right)^{-1}$$

then the uncertainty relation is simply expressed as:

$$\left(\frac{\sigma_T}{T}\right)^2 = \sum\left(\frac{\sigma_{N,i}}{N_T}\right)^2 \tag{A.7}$$

APPENDIX B

1D FLAME CODE DOCUMENTATION

Included here are short descriptions of the 1D flame codes that were modified or developed during the course of this work. The first code described, TUBEDIF, was modified to suit the author's needs and was previously developed out of the commercial code OPPDIF [61]. The other two codes, opprad_1D and oppaxi_1D, are based off of PETSc and were implemented during the development of the 2D cellular tubular code described in Chapter III.

B.1 TUBEDIF

This CHEMKIN-based code is used to simulate non-cellular tubular flames. This code is a modified version of OPPDIF [61], initially modified by Chih-Jen Sung for premixed flames (TUBEPRE [67]), and later modified by Mitchell Smooke for non-premixed flames (TUBEDIF [21]). During the course of this work, the two separate codes were combined for ease of use into TUBEDIF.

The velocity field is expressed in terms of the computational variables F, G, H:

$$F = -\rho r u \tag{B.1}$$

$$G = \rho r W \tag{B.2}$$

$$H = \frac{1}{z}\frac{\partial \widetilde{p}_1}{\partial z} \tag{B.3}$$

In implementation, the radial component of the momentum conservation equation is not solved. This reduces the computational expense of the simulation, at the loss of resolving the full dynamic pressure field $\widetilde{p}_1$. Since the pressure gradient that appears in the axial mo-

mentum conservation equation is an eigenvalue (H), the velocity field and flame structure (u, W, Y_i, T) may be resolved without knowledge of the complete dynamic pressure field.

The time-steady form of the conservation equations are then expressed in terms of the variables: F, G, Y_i, T, H. The governing equations are [12]: conservation of total mass,

$$0 = G - \frac{dF}{dr} \tag{B.4}$$

conservation of momentum in the axial direction,

$$0 = -\rho r F \frac{d}{dr}\left(\frac{G}{\rho r}\right) - \rho r \frac{d}{dr}\left[\mu r \frac{d}{dr}\left(\frac{G}{\rho r}\right)\right] + \rho r^2 H + G^2 \tag{B.5}$$

the eigenvalue equation,

$$0 = \frac{dH}{dr} \tag{B.6}$$

conservation of energy,

$$\begin{aligned} 0 = &-\frac{F}{r}\frac{dT}{dr} - \frac{1}{r c_p}\frac{d}{dr}\left(\lambda r \frac{dT}{dr}\right) + \frac{1}{c_p}\sum_{i\in\mathcal{S}}\left(\rho Y_i u_i^d c_{pi}\frac{dT}{dr}\right) \\ &+ \frac{1}{c_p}\sum_{i\in\mathcal{S}}\left(\omega_i h_i\right) + \frac{1}{c_p}Q - \frac{1}{r c_p}\frac{d}{dr}\left(r q^D\right) \end{aligned} \tag{B.7}$$

conservation of chemical species,

$$0 = -\frac{F}{r}\frac{dY_i}{dr} + \frac{1}{r}\frac{d}{dr}\left(r\rho Y_i u_i^d\right) - \omega_i W_i, \quad i \in \mathcal{S} \tag{B.8}$$

where u_i^d is the radial diffusion velocity of species i,

$$\rho Y_i u_i^d = \sum_{j\in\mathcal{S}}\left(Y_i \mathcal{D}_{ij}\frac{dx_j}{dr}\right) - Y_i \mathcal{D}_i^T \frac{1}{T}\frac{dT}{dr}, \quad i \in \mathcal{S} \tag{B.9}$$

`CHEMKIN` [48] is used to calculate the diffusive transport either in multicomponent form,

given in Equation 3.10, or mixture average form, given in Equation 3.11. Radiation heat loss (Q) is considered and is given by Equation 3.23.

For the premixed geometry, the problem domain is $r \in [0, R_o]$, where R_o is the outer nozzle radius. The boundary conditions for $r = 0$ are

$$\begin{aligned} F &= 0 & \tfrac{d}{dr}T &= 0 \\ \tfrac{d}{dr}G &= 0 & \tfrac{d}{dr}Y_k &= 0, \quad k \in \mathcal{S} \end{aligned}$$

and at $r = R_o$ are

$$\begin{aligned} F &= -\left(\rho R u\right)_{BC} & T &= T_{BC} \\ G &= \left(\rho R W\right)_{BC} & \rho Y_k \left(u + u_k^d\right) &= \left(\rho Y_k u\right)_{BC}, \quad k \in \mathcal{S} \end{aligned}$$

For the non-premixed geometry, the problem domain is $r \in [R_i, R_o]$. The boundary conditions for $r = R_i$ are

$$\begin{aligned} F &= -\left(\rho R u\right)_{BC} & \lambda \frac{dT}{dr} &= \sum_{k \in \mathcal{S}} \left(h|_T - h|_{T_{BC}}\right) \left(\rho u Y_k\right)_{BC} \\ G &= 0 & \rho Y_k \left(u + u_k^d\right) &= \left(\rho Y_k u\right)_{BC}, \quad k \in \mathcal{S} \end{aligned}$$

and the boundary conditions at $r = R_o$ is the same as for the premixed case.

B.1.1 Solution Algorithm

The governing system of equations is solved implicitly with `TWOPNT` [97]. The solver operates with two separate iterative algorithms to provide both global and fast local convergence. The local technique (damped inexact Newton's method) provides fast convergence for quick solve times, but only converges when the solution iterate is "close" to the final solution. The global technique (explicit pseudo-transient continuation) provides convergence

over a wider range of solution iterates, but suffers from slow convergence. The solution procedure is described in detail elsewhere [97–99]. In order to resolve the structure of the flame, adaptive gridding is used to place grid points preferentially at locations within the domain with high activity. Grid independence is confirmed by doubling the number of points and comparing the solutions.

B.2 `opprad_1D`

This `PETSc`-based code simulates the non-cellular tubular flame structure, which is provided by the existing `TUBEDIF`. The code is named `opprad_1D` for *opposed radial jets*, and may be used to simulate a flow domain both with or without an inner nozzle. From the boundary-layer assumption, the governing equations are simplified with the use of computational variables:

$$W = \frac{\partial w}{\partial z} \tag{B.10}$$

$$\widetilde{p}_1 = \frac{z^2}{2} H + I\left(r\right) \tag{B.11}$$

The time-steady form of the conservations equations are formulated in terms of the variables: u, W, H, I, Y_i, T. The governing equations are: conservation of total mass,

$$0 = \frac{\partial}{\partial r}\left(r\rho u\right) + r\rho W \tag{B.12}$$

conservation of momentum in the radial direction,

$$0 = \rho u \frac{\partial u}{\partial r} + \frac{\partial I}{\partial r} - \frac{1}{r}\frac{\partial}{\partial r}\left(2\mu r \frac{\partial u}{\partial r}\right) - \mu \frac{\partial W}{\partial r} + \frac{2\mu}{r}\frac{u}{r} \tag{B.13}$$

conservation of momentum in the axial direction,

$$0 = \rho\left(u\frac{\partial W}{\partial r} + W^2\right) + H - \frac{1}{r}\frac{\partial}{\partial r}\left(\mu r\frac{\partial W}{\partial r}\right) \tag{B.14}$$

the eigenvalue equation,

$$0 = \frac{dH}{dr} \tag{B.15}$$

conservation of energy,

$$\begin{aligned} 0 = {} & \rho u\frac{\partial T}{\partial r} + \frac{1}{rc_p}\frac{\partial}{\partial r}\left(rq_r - r\sum_{i\in\mathcal{S}} h_i\rho Y_i u_i^d\right) \\ & + \frac{1}{c_p}\sum_{i\in\mathcal{S}}\left(\rho Y_i u_i^d c_{pi}\frac{\partial T}{\partial r}\right) + \frac{1}{c_p}\sum_{i\in\mathcal{S}}\left(\omega_i h_i m_i\right) + \frac{Q}{c_p} \end{aligned} \tag{B.16}$$

and conservation of species,

$$0 = \rho u\frac{\partial Y_i}{\partial r} + \frac{1}{r}\frac{\partial}{\partial r}\left(r\rho u_i^d Y_i\right) - \omega_i m_i, \quad i \in \mathcal{S} \tag{B.17}$$

where the radial fluxes of heat (q_r) and mass ($\rho Y_i u_i^d$) are defined in Equation 3.8, and radiation heat loss (Q) is defined in Equation 3.23.

For the premixed geometry, the problem domain is $r \in [0, R_o]$, where R_o is the outer nozzle radius. The boundary conditions for $r = 0$ are

$$\begin{aligned} u &= 0 & \tfrac{d}{dr}T &= 0 \\ \tfrac{d}{dr}W &= 0 & \tfrac{d}{dr}Y_k &= 0, \quad k \in \mathcal{S} \end{aligned}$$

and at $r = R_o$ are

$$\begin{aligned} u &= u_{BC} & T &= T_{BC} \end{aligned}$$

$$W = W_{BC} \qquad \rho Y_k \left(u + u_k^d\right) = \left(\rho Y_k u\right)_{BC}, \quad k \in \mathcal{S}$$

For the non-premixed geometry, the problem domain is $r \in [R_i, R_o]$. The boundary conditions for $r = R_i$ are

$$\rho u = (\rho u)_{BC} \qquad \lambda \frac{dT}{dr} = \sum_{k \in \mathcal{S}} \left(h|_T - h|_{T_{BC}}\right) (\rho u Y_k)_{BC}$$

$$W = 0 \qquad \rho Y_k \left(u + u_k^d\right) = \left(\rho Y_k u\right)_{BC}, \quad k \in \mathcal{S}$$

and the boundary conditions at $r = R_o$ is the same as for the premixed case.

B.3 `oppaxi_1D`

This `PETSc`-based code simulates the non-cellular opposed jet flame structure, which is provided by the existing codes `OPPDIF` [61] or `CounterflowDiffusionFlame` from `Cantera` [49]. The code is named `oppaxi_1D` for *Opposed Axial Jets*, and may be used to simulate a general type of flame (not just a diffusion flame as popular naming convention seems to suggest). With the boundary-layer assumption, the domain is 1D along z and the governing equations are simplified with the use of computational variables:

$$U = \frac{u}{r} \tag{B.18}$$

$$\widetilde{p}_1 = \frac{r^2}{2} H + I(z) \tag{B.19}$$

The time-steady form of the conservations equations are formulated in terms of the variables: U, w, H, I, Y_i, T. The governing equations are: conservation of total mass,

$$0 = 2\rho U + \frac{\partial}{\partial z} (\rho w) \tag{B.20}$$

conservation of radial momentum,

$$0 = \rho U^2 + \rho w \frac{\partial U}{\partial z} + H - \frac{\partial}{\partial z}\left(\mu \frac{\partial U}{\partial z}\right) \tag{B.21}$$

conservation of axial momentum,

$$0 = \rho w \frac{\partial w}{\partial z} + \frac{\partial I}{\partial z} - 2\mu \frac{\partial U}{\partial z} - 2\frac{\partial}{\partial z}\left(\mu \frac{\partial w}{\partial z}\right) \tag{B.22}$$

the eigenvalue equation,

$$0 = \frac{dH}{dz} \tag{B.23}$$

conservation of energy,

$$\begin{aligned} 0 = \rho w \frac{\partial T}{\partial z} - \frac{1}{c_p}\frac{\partial}{\partial z}\left(r q_z - r \sum_{i \in \mathcal{S}} h_i \rho Y_i w_i^d\right) \\ + \frac{1}{c_p}\sum_{i \in \mathcal{S}}\left(\rho Y_i w_i^d c_{pi} \frac{\partial T}{\partial z}\right) + \frac{1}{c_p}\sum_{i \in \mathcal{S}}\left(\omega_i h_i m_i\right) + \frac{Q}{c_p} \end{aligned} \tag{B.24}$$

and conservation of chemical species,

$$0 = \rho w \frac{\partial Y_i}{\partial z} + \frac{\partial}{\partial z}\left(\rho Y_i w_i^d\right) - \omega_i m_i, \quad i \in \mathcal{S} \tag{B.25}$$

where the radial fluxes of heat and mass (q_z, $\rho Y_i w_i^d$) are defined in Equation 3.8, and radiation heat loss (Q) is defined in Equation 3.23.

For the premixed geometry, the problem domain is $z \in [0, L_o]$, where L_o is the spacing of the nozzle from the coordinate origin. The boundary conditions for $z = 0$ are

$$\begin{aligned} w &= 0 & \tfrac{d}{dz}T &= 0 \\ \tfrac{d}{dz}U &= 0 & \tfrac{d}{dz}Y_k &= 0, \quad k \in \mathcal{S} \end{aligned}$$

and at $z = L_o$ are

$$w = w_{BC} \qquad T = T_{BC}$$
$$U = U_{BC} \qquad \rho Y_k \left(w + w_k^d\right) = \left(\rho Y_k w\right)_{BC}, \quad k \in \mathcal{S}$$

For the non-premixed geometry, the problem domain is $z \in [L_i, L_o]$. The boundary conditions for $z = L_i$ are

$$w = w_{BC} \qquad T = T_{BC}$$
$$U = U_{BC} \qquad \rho Y_k \left(w + w_k^d\right) = \left(\rho Y_k w\right)_{BC}, \quad k \in \mathcal{S}$$

and the boundary conditions at $z = L_o$ is the same as for the premixed case.

REFERENCES

[1] H. Pitsch, "Large-eddy simulation of turbulent combustion," *Annual Review of Fluid Mechanics*, vol. 38, no. 1, pp. 453–482, 2006.

[2] N. Peters, "Laminar flamelet concepts in turbulent combustion," *Proceedings of the Combustion Institute*, vol. 21, pp. 1231–1250, 1988.

[3] J. Hirschfelder and C. Curtiss, "Theory of propagation of flames. Part I: General equations," *Symposium on Combustion and Flame, and Explosion Phenomena*, vol. 3, no. 1, pp. 121–127, 1948.

[4] M. D. Smooke, "The computation of laminar flames," *Proceedings of the Combustion Institute*, vol. 34, no. 1, pp. 65–98, 2013.

[5] M. Matalon, "Intrinsic flame instabilities in premixed and nonpremixed combustion," *Annual Review of Fluid Mechanics*, vol. 39, pp. 163–191, 2007.

[6] S. Ishizuka, D. Dunn-Rankin, R. W. Pitz, R. J. Kee, Y. Zhang, H. Zhu, T. Takeno, M. Nishioka, and D. Shimokuri, *Tubular Combustion*. New York: Momentum Press, LLC, 2013.

[7] Y. Wang, S. Hu, and R. W. Pitz, "Extinction and cellular instability of premixed tubular flames," *Proceedings of the Combustion Institute*, vol. 32, no. 1, pp. 1141–1147, 2009.

[8] C. K. Law, "Dynamics of stretched flames," *Proceedings of the Combustion Institute*, vol. 21, pp. 1381–1402, 1988.

[9] L. de Goey and J. ten Thije Boonkkamp, "A Mass-Based Definition of Flame Stretch for Flames with Finite Thickness," *Combustion Science and Technology*, vol. 122, pp. 399–405, 1997.

[10] L. de Goey, R. Mallens, and J. Ten Thije Boonkkamp, "An evaluation of different contributions to flame stretch for stationary premixed flames," *Combustion and Flame*, vol. 110, pp. 54–66, 1997.

[11] H. Schlicting, "Exact solutions of the Navier-Stokes equations," in *Boundary-Layer Theory*, pp. 95–99, New York: McGraw Hill, 7 ed., 1979.

[12] P. Wang, J. A. Wehrmeyer, and R. W. Pitz, "Stretch rate of tubular premixed flames," *Combustion and Flame*, vol. 145, no. 1-2, pp. 401–414, 2006.

[13] R. W. Pitz, S. Hu, and P. Wang, "Tubular premixed and diffusion flames: Effect of stretch and curvature," *Progress in Energy and Combustion Science*, vol. 42, pp. 1–34, 2014.

[14] S. Hu, P. Wang, and R. W. Pitz, "A structural study of premixed tubular flames," *Proceedings of the Combustion Institute*, vol. 32, no. 1, pp. 1133–1140, 2009.

[15] S. Ishizuka, "Characteristics of tubular flames," *Progress in Energy and Combustion Science*, vol. 19, pp. 187–226, 1993.

[16] C. Law and C. Sung, "Structure, aerodynamics, and geometry of premixed flamelets," *Progress in Energy and Combustion Science*, vol. 26, pp. 459–505, 2000.

[17] A. C. Eckbreth, *Laser Diagnostics for Combustion Temperature and Species*. Gordon and Breach Publishers, 2 ed., 1996.

[18] S. Hu, *Measurements and modeling of non-premixed tubular flames: structure, extinction and instability*. Ph.D. thesis, Vanderbilt University, 2007.

[19] G. P. Smith, J. Luque, C. Park, J. B. Jeffries, and D. R. Crosley, "Low pressure flame determinations of rate constants for OH(A) and CH(A) chemiluminescence," *Combustion and Flame*, vol. 131, pp. 59–69, 2002.

[20] D. Long, *The Raman Effect: A Unified Treatment of the Theory of Raman Scattering by Molecules*. John Wiley & Sons, Inc., 2002.

[21] S. Hu, P. Wang, R. W. Pitz, and M. D. Smooke, "Experimental and numerical investigation of non-premixed tubular flames," *Proceedings of the Combustion Institute*, vol. 31, pp. 1093–1099, 2007.

[22] J. Kojima and Q.-V. Nguyen, "Laser pulse-stretching with multiple optical ring cavities.," *Applied Optics*, vol. 41, pp. 6360–70, 2002.

[23] R. J. Osborne, P. A. Skaggs, and R. W. Pitz, "Multi-camera/spectrometer design for instantaneous line Rayleigh/Raman/LIPF measurements in methane/air flames," in *AIAA 96-0175*, 1996.

[24] R. W. Dibble, S. H. Starner, A. R. Masri, and R. S. Barlow, "An improved method of data aquisition and reduction for laser Raman-Rayleigh and fluorescence scattering from multispecies," *Applied Physics B Photophysics and Laser Chemistry*, vol. 51, pp. 39–43, 1990.

[25] D. Geyer, *1D Raman/Rayleigh experiments in a turbulent opposed jet*. Ph.D. thesis, TU Darmstadt, Düsseldorf, Germany, 2005.

[26] W. Hill and D. Rogalla, "Spike-correction of weak signals from charge-coupled devices and its application to Raman spectroscopy," *Analytical Chemistry*, vol. 64, pp. 2575–2579, 1992.

[27] G. Schulze, A. Jirasek, M. M. L. Yu, A. Lim, R. F. B. Turner, and M. W. Blades, "Investigation of selected baseline removal techniques as candidates for automated implementation," *Applied Spectroscopy*, vol. 59, pp. 545–574, 2005.

[28] C. A. Lieber and A. Mahadevan-Jansen, "Automated method for subtraction of fluorescence from biological Raman spectra.," *Applied Spectroscopy*, vol. 57, pp. 1363–7, 2003.

[29] H. Ruan and L. K. Dai, "Automated background subtraction algorithm for Raman spectra based on iterative weighted least squares," *Asian Journal of Chemistry*, vol. 23, no. 12, pp. 5229–5234, 2011.

[30] C. A. Hall, W. D. Kulatilaka, J. R. Gord, and R. W. Pitz, "Quantitative atomic hydrogen measurements in premixed hydrogen tubular flames," *Combustion and Flame*, vol. 161, pp. 2924–2932, 2014.

[31] K. Kohse-Höinghaus, "Laser techniques for the quantitative detection of reactive intermediates in combustion systems," *Progress in Energy and Combustion Science*, vol. 20, pp. 203–279, 1994.

[32] P. Paul, "A model for temperature-dependent collisional quenching of OH $A^2\ \Sigma^+$," *Journal of Quantitative Spectroscopy and Radiative Transfer*, vol. 51, pp. 511–524, 1994.

[33] N. M. Laurendeau, *Statistical Thermodynamics*. Cambridge University Press, 2010.

[34] S. J. Kline and F. A. McClintock, "Describing uncertainties in single-sample experiments," *Mechanical Engineering*, vol. 75, pp. 3–8, 1953.

[35] W. D. Kulatilaka, J. H. Frank, B. D. Patterson, and T. B. Settersten, "Analysis of 205 nm photolytic production of atomic hydrogen in methane flames," *Applied Physics B*, vol. 97, pp. 227–242, 2009.

[36] W. D. Kulatilaka, J. R. Gord, V. R. Katta, and S. Roy, "Photolytic-interference-free, femtosecond two-photon fluorescence imaging of atomic hydrogen," *Optics Letters*, vol. 37, pp. 3051–3053, 2012.

[37] W. Kulatilaka, J. Gord, and S. Roy, "Femtosecond two-photon LIF imaging of atomic species using a frequency-quadrupled Ti:sapphire laser," *Applied Physics B*, vol. 116, no. 1, pp. 7–13, 2014.

[38] W. D. Kulatilaka, J. H. Frank, and T. B. Settersten, "Interference-free two-photon LIF imaging of atomic hydrogen in flames using picosecond excitation," *Proceedings of the Combustion Institute*, vol. 32, pp. 955–962, 2009.

[39] C. D. Claxton and R. C. Staunton, "Measurement of the point-spread function of a noisy imaging system," *Journal of the Optical Society of America A*, vol. 25, pp. 159–170, 2008.

[40] T. E. Gureyev, Y. I. Nesterets, A. W. Stevenson, and S. W. Wilkins, "A method for local deconvolution.," *Applied Optics*, vol. 42, pp. 6488–94, 2003.

[41] J. Bittner, K. Kohse-höinghaus, U. Meier, and T. Just, "Quenching of two-photon-excited H(3s, 3d) and O(3p $^3P_{2,1,0}$) atoms by rare gases and small molecules," *Chemical Physics Letters*, vol. 143, pp. 571–576, 1988.

[42] U. Meier, K. Kohse-Höinghaus, and T. Just, "H and O atom detection for combustion applications: study of quenching and laser photolysis effects," *Chemical Physics Letters*, vol. 126, no. 6, pp. 567–573, 1986.

[43] W. D. Kulatilaka, R. P. Lucht, S. F. Hanna, and V. R. Katta, "Two-color, two-photon laser-induced polarization spectroscopy (LIPS) measurements of atomic hydrogen in near-adiabatic, atmospheric pressure hydrogen/air flames," *Combustion and Flame*, vol. 137, pp. 523–537, 2004.

[44] R. B. Bird, W. E. Stewart, and E. N. Lightfoot, *Transport Phenomena*. New York: John Wiley & Sons, Inc., 2 ed., 2007.

[45] V. Giovangigli, *Multicomponent Flow Modeling*. Boston: Birkhaeuser, 1999.

[46] A. Ern and V. Giovangigli, "Fast and accurate multicomponent transport property evaluation," *Journal of Computational Physics*, vol. 120, pp. 105–116, 1995.

[47] R. J. Kee, F. M. Rupley, E. Meeks, and J. A. Miller, "Chemkin-II: A Fortran chemical kinetics package for the analysis of gas-phase chemical and plasma kinetics," in *SAND89-8009*, 1989.

[48] R. J. Kee, G. Dixon-Lewis, J. Warnatz, M. E. Coltrin, J. A. Miller, and H. K. Moffat, "Transport: A Fortran computer code package for the evaluation of gas-phase, multicomponent transport properties," in *SAND86-8246B*, 1986.

[49] D. Goodwin, "Cantera: An object-oriented software toolkit for chemical kinetics, thermodynamics, and transport processes," 2013. http://code.google.com/p/cantera/.

[50] R. J. Kee, M. E. Coltrin, and P. Glarborg, *Chemically Reacting Flow*. Hoboken, NJ, USA: John Wiley & Sons, Inc., 2003.

[51] I. Glassman and R. A. Yetter, *Combustion*. Boston: Elsevier Inc., 4th ed., 2008.

[52] M. P. Burke, M. Chaos, Y. Ju, F. L. Dryer, and S. J. Klippenstein, "Comprehensive H_2/O_2 kinetic model for high-pressure combustion," *International Journal of Chemical Kinetics*, vol. 44, pp. 444–474, 2012.

[53] J. Li, Z. Zhao, A. Kazakov, M. Chaos, F. L. Dryer, and J. J. Scire, "A comprehensive kinetic mechanism for CO, CH_2O, and CH_3OH combustion," *International Journal of Chemical Kinetics*, vol. 39, pp. 109–136, 2007.

[54] J. O. Hirschfelder, C. F. Curtiss, and R. B. Bird, *Molecular Theory of Gases and Liquids*. Wiley-Interscience, 1964.

[55] K. Yamamoto, T. Hirano, and S. Ishiuka, "Effects of pressure diffusion on the characteristics of tubular flames," *Proceedings of the Combustion Institute*, vol. 26, pp. 1129–1135, 1996.

[56] A. Ern and V. Giovangigli, "Impact of detailed multicomponent transport on planar and counterflow hydrogen/air and methane/air flames," *Combustion Science and Technology*, vol. 149, pp. 157–181, 1999.

[57] A. Ern and V. Giovangigli, "Thermal diffusion effects in hydrogen-air and methane-air flames," *Combustion Theory and Modelling*, vol. 2, pp. 349–372, 1998.

[58] G. Billet, V. Giovangigli, and G. de Gassowski, "Impact of volume viscosity on a shock-hydrogen-bubble interaction," *Combustion Theory and Modelling*, vol. 12, pp. 221–248, 2008.

[59] A. Ern and V. Giovangigli, *Multicomponent Transport Algorithms*, vol. 24 of *Lecture Notes in Physics Monographs*. Berlin, Heidelberg: Springer-Verlag, 1994.

[60] V. Giovangigli, "Multicomponent transport in laminar flames," *Proceedings of the Combustion Institute*, vol. 35, no. 1, pp. 625–637, 2015.

[61] A. E. Lutz, R. J. Kee, J. F. Grcar, and F. M. Rupley, "OPPDIF: A Fortran program for computing opposed-flow diffusion flames," in *SAND96-8243*, 1997.

[62] U. Niemann, K. Seshadri, and F. A. Williams, "Accuracies of laminar counterflow flame experiments," *Combustion and Flame*, vol. 162, pp. 1540–1549, 2015.

[63] J. M. Bergthorson, K. Sone, T. W. Mattner, P. E. Dimotakis, D. G. Goodwin, and D. I. Meiron, "Impinging laminar jets at moderate Reynolds numbers and separation distances," *Physical Review E - Statistical, Nonlinear, and Soft Matter Physics*, vol. 72, no. 6, pp. 1–12, 2005.

[64] C. Frouzakis, J. Lee, A. Tomboulides, and K. Boulouchos, "Two-dimensional direct numerical simulation of opposed-jet hydrogen-air diffusion flame," *Proceedings of the Combustion Institute*, vol. 27, pp. 571–577, 1998.

[65] B. Sarnacki, G. Esposito, R. Krauss, and H. Chelliah, "Extinction limits and associated uncertainties of nonpremixed counterflow flames of methane, ethylene, propylene and n-butane in air," *Combustion and Flame*, vol. 159, pp. 1026–1043, 2012.

[66] H. Kobayashi and M. Kitano, "Flow fields and extinction of stretched cylindrical premixed flames," *Combustion Science and Technology*, vol. 75, pp. 227–239, 1991.

[67] D. M. Mosbacher, J. A. Wehrmeyer, R. W. Pitz, C.-J. Sung, and J. L. Byrd, "Experimental and numerical investigation of premixed tubular flames," *Proceedings of the Combustion Institute*, vol. 29, pp. 1479–1486, 2002.

[68] M. D. Smooke and V. Giovangigli, "Extinction of tubular premixed laminar flames with complex chemistry," *Proceedings of the Combustion Institute*, vol. 23, pp. 447–454, 1990.

[69] R. Barlow, A. Karpetis, J. Frank, and J.-Y. Chen, "Scalar profiles and NO formation in laminar opposed-flow partially premixed methane/air flames," *Combustion and Flame*, vol. 127, pp. 2102–2118, 2001.

[70] Y. Xu, M. D. Smooke, P. Lin, and M. B. Long, "Primitive variable modeling of multidimensional laminar flames," *Combustion Science and Technology*, vol. 90, no. 5, pp. 289–313, 1993.

[71] S. V. Patankar, *Numerical Heat Transfer and Fluid Flow*. New York: Hemisphere Publishing Corp., 1980.

[72] B. Fornberg, "Generation of finite difference formulas on arbitrarily spaced grids," *Mathematics of Computation*, vol. 51, pp. 699–706, 1988.

[73] M. D. Smooke, "Solution of burner-stabilized premixed laminar flames by boundary value methods," *Journal of Computational Physics*, vol. 48, pp. 72–105, 1982.

[74] B. A. V. Bennett and M. D. Smooke, "Local rectangular refinement with application to nonreacting and reacting fluid flow problems," *Journal of Computational Physics*, vol. 151, pp. 684–727, 1999.

[75] M. S. Day and J. B. Bell, "Numerical simulation of laminar reacting flows with complex chemistry," *Combustion Theory and Modelling*, vol. 4, pp. 535–556, 2000.

[76] T. S. Coffey, C. T. Kelley, and D. E. Keyes, "Pseudotransient continuation and differential-algebraic equations," *SIAM Journal on Scientific Computing*, vol. 25, pp. 553–569, 2003.

[77] P. R. McHugh, D. A. Knoll, and D. E. Keyes, "Application of Newton-Krylov-Schwarz algorithm to low-Mach-number compressible combustion," *AIAA Journal*, vol. 36, pp. 290–292, 1998.

[78] D. A. Knoll, P. R. McHugh, and D. E. Keyes, "Newton-Krylov methods for low-Mach-number compressible combustion," *AIAA Journal*, vol. 34, pp. 961–967, 1996.

[79] X.-C. Cai and M. Sarkis, "A restricted additive Schwarz preconditioner for general sparse linear systems," *SIAM Journal on Scientific Computing*, vol. 21, no. 2, pp. 792–797, 1999.

[80] S. Balay, W. D. Gropp, L. C. McInnes, and B. F. Smith, "The Portable Extensible Toolkit for Scientific Computing," 2015. http://www.mcs.anl.gov/petsc/.

[81] L. Tosatto, B. A. V. Bennett, and M. D. Smooke, "Parallelization strategies for an implicit Newton-based reactive flow solver," *Combustion Theory and Modelling*, vol. 15, no. 4, pp. 455–486, 2011.

[82] H. Chelliah, C. Law, T. Ueda, M. Smooke, and F. Williams, "An experimental and theoretical investigation of the dilution, pressure and flow-field effects on the extinction condition of methane-air-nitrogen diffusion flames," *Proceedings of the Combustion Institute*, vol. 23, pp. 503–511, 1991.

[83] R. Franke, "Scattered data interpolation: tests of some methods," *Mathematics of Computation*, vol. 38, no. 157, pp. 181–181, 1982.

[84] B. Fornberg and G. Wright, "Stable computation of multiquadric interpolants for all values of the shape parameter," *Computers and Mathematics with Applications*, vol. 48, no. 5-6, pp. 853–867, 2004.

[85] S. A. Sarra and E. J. Kansa, "Multiquadric radial basis function approximation methods for the numerical solution of partial differential equations," *Advances in Computational Mechanics*, vol. 2, p. 2009, 2009.

[86] D. Bradley, M. Haq, R. Hicks, T. Kitagawa, M. Lawes, C. Sheppard, and R. Woolley, "Turbulent burning velocity, burned gas distribution, and associated flame surface definition," *Combustion and Flame*, vol. 133, pp. 415–430, 2003.

[87] C. A. Hall and R. W. Pitz, "A structural study of premixed hydrogen-air cellular tubular flames," *Proceedings of the Combustion Institute*, vol. 34, pp. 973–980, 2013.

[88] K. T. Aung, M. I. Hassan, and G. M. Faeth, "Flame stretch interactions of laminar premixed hydrogen / air flames at normal temperature and pressure," *Combustion and Flame*, vol. 109, pp. 1–24, 1997.

[89] V. N. Kurdyumov, "Diffusive-thermal instability of premixed tubular flames," *Combustion and Flame*, vol. 158, pp. 1718–1726, 2011.

[90] G. J. Sharpe and S. A. E. G. Falle, "Nonlinear cellular instabilities of planar premixed flames: numerical simulations of the reactive Navier–Stokes equations," *Combustion Theory and Modelling*, vol. 10, pp. 483–514, 2006.

[91] R. Seydel, *From Equilibrium to Chaos: Practical Bifurcation and Stability Analysis*. New York: Elsevier Inc., 1988.

[92] J. van Oijen, R. Bastiaans, and L. de Goey, "Low-dimensional manifolds in direct numerical simulations of premixed turbulent flames," *Proceedings of the Combustion Institute*, vol. 31, pp. 1377–1384, 2007.

[93] F. Yang, C. Law, C. Sung, and H. Zhang, "A mechanistic study of Soret diffusion in hydrogen–air flames," *Combustion and Flame*, vol. 157, pp. 192–200, 2010.

[94] J. Grcar, J. Bell, and M. Day, "The Soret effect in naturally propagating, premixed, lean, hydrogen–air flames," *Proceedings of the Combustion Institute*, vol. 32, no. 1, pp. 1173–1180, 2009.

[95] J. de Charentenay and A. Ern, "Multicomponent transport impact on turbulent premixed H_2/O_2 flames," *Combustion Theory and Modelling*, vol. 6, pp. 439–462, 2002.

[96] R. J. Kee, J. F. Grcar, M. D. Smooke, and J. A. Miller, "PREMIX: A Fortran program for modeling steady one-dimensional premixed flames," in *SAND85-8240*, 1985.

[97] J. F. Grcar, "The Twopnt program for boundary value problems," in *SAND91-8230*, 1991.

[98] R. J. Kee, J. A. Miller, G. H. Evans, and G. Dixon-Lewis, "A computational model of the structure and extinction of strained, opposed flow, premixed methane-air flames," *Proceedings of the Combustion Institute*, vol. 22, pp. 1479–1494, 1989.

[99] J. E. J. Dennis and R. B. Schnabel, *Numerical Methods for Unconstrained Optimization and Nonlinear Equations*. New Jersey: Prentice-Hall, Inc., 1983.